REVIEW

Check for updates

Yolk–shell nanostructures: synthesis, photocatalysis and interfacial charge dynamics

Yi-An Chen,[†a] Yu-Ting Wang,[†a] Hyun Sik Moon,[b] Kijung Yong [ID][b] and Yung-Jung Hsu [ID] *[acd]

Solar energy has long been regarded as a promising alternative and sustainable energy source. In this regard, photocatalysts emerge as a versatile paradigm that can practically transform solar energy into chemical energy. At present, unsatisfactory conversion efficiency is a major obstacle to the widespread deployment of photocatalysis technology. Many structural engineering strategies have been proposed to address the issue of insufficient activity for semiconductor photocatalysts. Among them, creation of yolk–shell nanostructures which possess many beneficial features, such as large surface area, efficient light harvesting, homogeneous catalytic environment and enhanced molecular diffusion kinetics, has attracted particular attention. This review summarizes the developments that have been made for the preparation and photocatalytic applications of yolk–shell nanostructures. Additional focus is placed on the realization of interfacial charge dynamics and the possibility of achieving spatial separation of charge carriers for this unique nanoarchitecture as charge transfer is the most critical factor determining the overall photocatalytic efficiency. A future perspective that can facilitate the advancement of using yolk–shell nanostructures in sophisticated photocatalytic systems is also presented.

[a]Department of Materials Science and Engineering, National Chiao Tung University, Hsinchu 30010, Taiwan. E-mail: yhsu@cc.nctu.edu.tw

[b]Surface Chemistry Laboratory of Electronic Materials, Department of Chemical Engineering, Pohang University of Science and Technology (POSTECH), Pohang 790-784, Korea

[c]Center for Emergent Functional Matter Science, National Chiao Tung University, Hsinchu 30010, Taiwan

[d]Department of Materials Science and Engineering, National Yang Ming Chiao Tung University, Hsinchu 30010, Taiwan

† These authors contributed equally.

1. Introduction

The past decade has witnessed an urgent demand for alternative energy, which has prompted academia and industry to devote effort to green energy technology. The sun is one of the essential elements for human life, and it can be regarded as an almost inexhaustible clean, renewable energy source. The difficulty is how to utilize this natural source efficiently. Photocatalysts are media which can convert solar energy into chemical energy. This feature makes photocatalysis competitive among different energy conversion technologies. H_2, O_2 and

Yi-An Chen received her bachelor's degree from the Department of Materials Science and Engineering at National Chiao Tung University in Taiwan in 2019. Currently, she is pursuing her PhD degree under the supervision of Prof. Yung-Jung Hsu in the Department of Materials Science and Engineering at National Chiao Tung University. She specializes in the synthesis and characterizations of hollow nanostructures comprising metals and semiconductors as well as applications in the fields of photoconversion and electrochemistry.

Yu-Ting Wang received her bachelor's degree in Materials Science and Engineering from National Chiao Tung University, Taiwan, in 2019. She is presently a PhD student in the Department of Materials Science and Engineering at National Chiao Tung University under the supervision of Prof. Yung-Jung Hsu. She is currently working on the research topic of TiO2-based nanocomposites and their applications in photocatalysis.

hydrocarbons, which can be obtained by photocatalytic water splitting[1,2] and CO_2 reduction,[3,4] respectively, are considered as potential alternative fuels to replace fossil fuels. No matter how these alternative fuels are consumed, the products after usage are clean and eco-friendly, complying with the core concept of sustainable development. In addition to producing green fuels, photocatalysis can also be operated to conduct wastewater treatment[5,6] and environmental remediation.[7,8] Using photocatalysts to decompose organic substances (*e.g.* antibiotics, dyes, bacteria) and inorganic toxicants (*e.g.* heavy metal ions, salt anions) is particularly attractive as it provides a feasible solution to the headache of the ever-rising universal environmental change. Moreover, photocatalysis can mediate the high costs and complicated processing in the manufacture of value-added chemicals.[9,10] Continuous effort has been devoted to the production of high value-added organic compounds by photocatalytic reactions.

The mechanism of photocatalysis can be divided into three primary steps. The first is to apply light irradiation with sufficient energy to semiconductor photocatalysts; the second is the generation of electron–hole pairs and the subsequent charge carrier transfer; the third comprises the occurrence of surface redox reactions mediated by photoexcited electrons and holes. From a thermodynamics point of view, the photoexcited electrons must have a sufficiently high reducing power in order to manage the desired reduction reactions. In other words, the conduction band (CB) level of the selected photocatalyst must be located at a potential more cathodic than the potential required for the reduction reactions. Similarly, the valence band (VB) level of semiconductor should lie in an adequately anodic potential to endow photoexcited holes with enough oxidizing power capable of conducting oxidation reactions. During the photocatalytic process, there however exist many handicaps that can result in low photocatalytic activity. These disservices include poor light absorption, rapid electron–hole recombination, and sluggish charge transfer kinetics. As dragged by such feet of clay, only a limited amount of charge carriers can actually participate in surface redox reactions. This dilemma could be ameliorated by designing composite photocatalysts with well-defined structural and compositional heterogeneity, in which the attributes of individual components can be combined. Much significantly, integrating multiple components to create heterojunction can modify electronic band structure, rectifying charge transfer behavior to increase carrier utilization efficiency. Till now, various composite nanostructures have been proposed as the photocatalyst paradigm to construct superior photocatalytic systems. Representative examples are doped/alloyed nanocrystals,[11–16] particle-decorated nanostructures,[17–40] heterodimers,[41] core–shell nanocrystals,[42–47] and yolk–shell nanostructures.[48,49] Here, yolk–shell nanostructures stand for a newly emerging photocatalyst platform, which are composed of a movable core surrounded by a permeable shell with void space. Such a peculiar architecture possesses several noteworthy advantages, including confined space which can facilitate the diffusion of reacting species, and large surface area which can provide abundant active sites. Besides, the incident light may undergo multiple reflections inside the void space and thus conduce to photon harvesting. Most

Hyun Sik Moon received his BSc in Nanotechnology Engineering from the University of Waterloo, Canada. He has been a PhD candidate in the Department of Chemical Engineering at Pohang University of Science and Technology, South Korea, under the supervision of Prof. Kijung Yong since 2018. His current research focuses on the synthesis of photocatalytic nanomaterials and their application to solar-fuel production.

Kijung Yong received his BS and MS in Chemical Engineering from Yonsei University, Korea; his PhD in Chemical Engineering from Carnegie Mellon University. After his postdoctoral fellow at University of Texas at Austin, he is currently a professor in the Department of Chemical Engineering, Pohang University of Science and Technology, South Korea, and an Editor of Applied Surface Science (Elsevier). His research expertise is in surface chemistry, wettability control and design of inorganic materials for solar energy conversion.

Yung-Jung Hsu is a Professor at the Department of Materials Science and Engineering, National Chiao Tung University, Taiwan. He received his bachelor's degree and PhD degree in Chemical Engineering from National Tsing Hua University in Taiwan. After working as a postdoctoral fellow at National Tsing Hua University, he joined National Chiao Tung University and started an independent research career in 2007. His research interests include design of advanced nanostructures, investigation of interfacial charge carrier dynamics and development of renewable energy technology.

importantly, the electronic band alignment between yolk and shell components can induce effective separation of photoexcited electrons and holes, which is an indispensable feature for superior photocatalytic efficiency.

Considerable effort in recent years has been made to devise feasible synthetic approaches to yolk–shell nanostructures and demonstrate their practice in photocatalytic applications. As illustrated in Scheme 1, this review gives a comprehensive retrospection on the preparation and photocatalytic applications of yolk–shell nanostructures. Additional focus is placed on the realization of interfacial charge dynamics and the possibility of achieving spatial separation of charge carriers for this unique nanoarchitecture as charge transfer is the most critical factor determining the overall photocatalytic efficiency. The review ends with a summary and future perspective that can facilitate the advancement of using yolk–shell nanostructures in sophisticated photocatalytic systems. For readers who are interested in acquiring the development of photocatalysts technology based on other types of composite nanostructures, we recommend some recent review articles.[50–58]
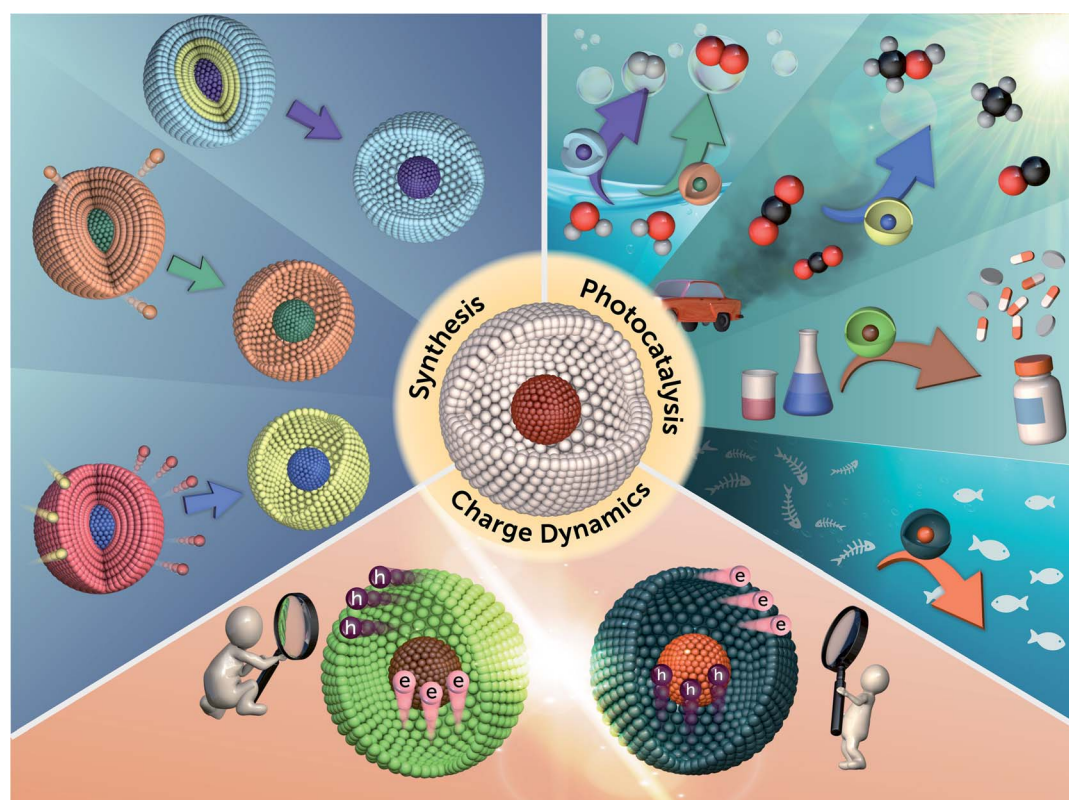
2. Synthetic approach

Base on the mechanism of void space formation, the synthetic approach to yolk–shell nanostructures can be divided into five categories. Kirkendall effect and galvanic replacement are both relevant to ion exchange, but the former is derived from different solubility products and the latter is caused by distinct redox potentials. Ostwald ripening is a crystal growth process involving the dissolution of particles with smaller size for deposition on larger particles. This process can be exploited to produce void space as the dissolved particles contract. Chemical etching creates void space at the expense of sacrificial templates by selective etching. Hollow structure can also be generated through physical volatilization or oxidative decomposition by means of thermal treatment. The following section further describes the details of these synthetic systems.

2.1 Kirkendall effect

Diffusion couple has been widely exploited to synthesize hollow structure. On account of the different diffusion rates, voids can be generated as two ions encounter, which is known as Kirkendall effect. At present, plenty of works have adopted this principle to prepare for yolk–shell nanostructures with various compositions, e.g. Se–SnO$_2$,[59] Sn/Sn$_2$Co$_3$–CoSnO$_3$/Co$_3$O$_4$,[60] Pt–CoO,[61] Au–Fe$_3$O$_4$[62] and Au–CdS.[63] Chiu et al. successfully demonstrated the growth of Au–CdS yolk–shell nanostructures by Kirkendall effect.[63] The experimental procedure is shown in Fig. 1A. The citrate-protected Au nanoparticles (NPs) were first subjected to coordination of Cu^{2+} ions via the surface carboxyl groups. A uniform layer of Cu$_2$O can then be coated on each of the Au NPs to produce Au–Cu$_2$O core–shell NP template. Next, Na$_2$S was added to the Au–Cu$_2$O suspension, transforming Cu$_2$O shell into Cu$_7$S$_4$ as a result of the lower solubility product of Cu$_7$S$_4$ than Cu$_2$O. In addition to the compositional change,

Scheme 1 Schematic illustration for the synthesis, photocatalysis and charge dynamics of yolk–shell nanostructures.
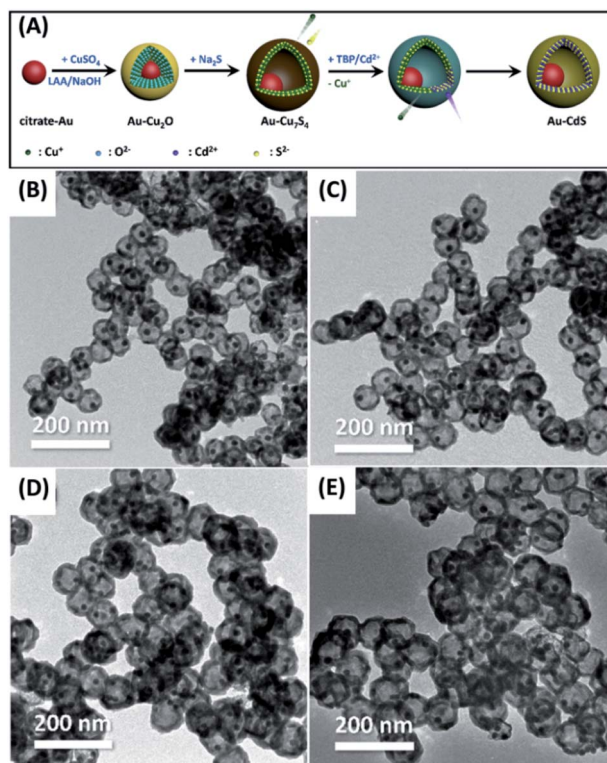
Fig. 1 (A) Synthetic approach to Au–CdS yolk–shell nanostructures by Kirkendall effect. (B–E) TEM images of Au–CdS with increasing void sizes. Reproduced with permission from ref. 63. Copyright 2019, Elsevier.
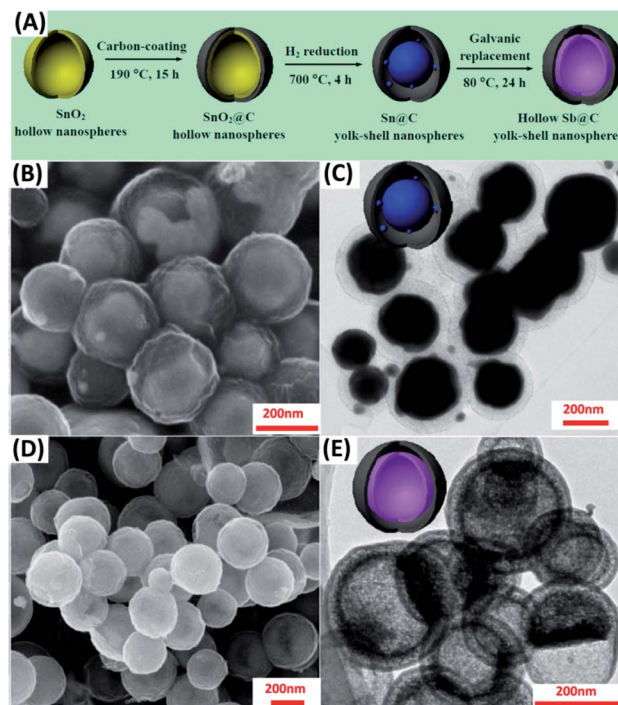

Fig. 2 (A) Synthetic approach to Sb–C yolk–shell nanospheres by galvanic replacement. (B and C) SEM and TEM images for Sn–C. (D and E) SEM and TEM images for Sb–C. Reproduced with permission from ref. 67. Copyright 2017, American Chemical Society.

Kirkendall voids were also generated at the shell layer by virtue of the faster outward diffusion of Cu^{2+} relative to the inward diffusion of S^{2-}. Lastly, cation exchange was performed to convert Cu_7S_4 to CdS, producing Au–CdS yolk–shell nanostructures. Notably, changing the Au NP/Cu^{2+} ratio during the synthesis of Au–Cu_2O template can produce Au–CdS with controllable void size. Fig. 1B–E shows the TEM images of Au–CdS with increasing void sizes from 40.2 ± 3.3 nm to 64.0 ± 6.3 nm. These yolk–shell nanostructures all possessed a constant shell thickness of around 11.5 ± 0.4 nm. Overall, Kirkendall effect represents a potentially universal strategy for the synthesis of yolk–shell nanostructures. As long as the difference in solubility product is deliberately considered, yolk–shell nanostructures with desired compositions can be obtained.

2.2 Galvanic replacement

By choosing two elements with suitable oxidation and reduction potentials, the replacement reaction can occur spontaneously. This principle is generally used to fabricate yolk–shell nanostructures with a wide range of compositions, including Ni–SnO_2/Ni_3Sn_2,[64] Co–Au,[65] Au–AgPd,[66] Sb–C[67] and Pd–M_xCu_{1-x} (M = Au, Pd, and Pt).[68] Liu *et al.* ingeniously designed hollow Sb–C yolk–shell spheres from Sn–C yolk–shell structures *via* galvanic replacement.[67] Fig. 2A displays the synthetic process. Hollow SnO_2 nanospheres were first obtained in the hydrothermal

reaction, followed by the uniform coating of a carbon shell. Further annealing under H_2 can convert hollow SnO_2 to solid Sn particles with empty space left between carbon shell and Sn core. Because Sb has a larger reducing potential than Sn ($E_{Sb^{3+}/Sb}$ = 0.241 V *vs.* SHE; $E_{Sn^{4+}/Sn}$ = 0.0129 V *vs.* SHE), adding Sb^{3+} can further transform Sn–C to Sb–C. In this galvanic replacement process, Sn was oxidized to Sn^{4+}, while Sb^{3+} was reduced to Sb; meanwhile, structural transformation from solid Sn to hollow Sb occurred owing to the non-equilibrium of ion diffusion between outward Sn^{4+} (faster) and inward Sb^{3+} (slower). The microstructure of Sn–C and Sb–C was explored with scanning electron microscopy (SEM) and transmission electron microscopy (TEM). As Fig. 2B–E show, Sb–C inherited the size and morphology from the parent Sn–C. The solid Sn core in Sn–C and hollow Sb yolk in Sb–C can also be clearly identified. Analogous to Kirkendall effect, galvanic replacement is a general approach to the synthesis of yolk–shell nanostructures. By pairing up suitable redox potentials, yolk–shell nanostructures with a wide range of materials combination can be readily obtained.

2.3 Ostwald ripening

Ostwald ripening can account for the growth of yolk–shell nanostructures possessing single composition (homogeneous) or multiple compositions (heterogeneous). The formation of homogeneous yolk–shell structures involves the dissolution of a core particle and re-deposition of a shell layer on the gradually dissolved core. Heterogeneous yolk–shell structures on the

other hand grow when core particle or shell layer itself dissolves and re-crystalizes. Because of the fascinating, synergistic properties, more attention has been paid to the synthesis of heterogeneous yolk–shell nanostructures, for instance, ZnO–C,[69] Au–TiO_2,[70] Fe_3O_4–Co_3O_4[71] and N-doped TiO_2–C.[72] Zhang et al. proposed an Ostwald ripening-based solvothermal system to prepare for N-doped TiO_2–C yolk–shell spheres.[72] The formation mechanism is depicted in Fig. 3A. TiO_2 spheres were first grown from the aggregation and self-assembly of small TiO_2 nuclei, which were simultaneously doped by N, wrapped by C and dissolved in a ripening process. Here, the addition of diethylenetriamine (DETA) as the coordinating reagent was crucial for inducing Ostwald ripening. If DETA was not added in the solvothermal reaction, solid spheres of TiO_2 were otherwise obtained. Fig. 3B and C and D and E respectively show the SEM and TEM images for solid TiO_2 and N-doped TiO_2–C yolk–shell spheres. Solid TiO_2 spheres had a size ranging from 1.0 to 1.5 μm, while N-doped TiO_2–C had a mean diameter of 600–700 nm. It is generally believed that minimization of surface energy is the main cause for driving Ostwald ripening. However, the exact systematic factors of inducing ripening process remain uncontrollable.

2.4 Chemical etching

Among different ways to fabricate yolk–shell nanostructures, template-assisted method represents the most straightforward approach. As long as an extra layer of etchable materials (mostly SiO_2) is coated between the core and shell components, followed by selective etching to remove this layer, an empty space can be generated between the core and shell. This chemical etching concept can be adopted to prepare for a variety of yolk–shell nanostructures, such as Au–RGO/TiO_2,[73] Ag/TiO_2–SiO_2,[74] Au–TiO_2,[75] Bi–SnO_2[76] and multi-shell TiO_2.[77] Hwang et al. synthesized multi-shell TiO_2 hollow NPs by using the chemical etching method.[77] Fig. 4A presents a scheme of the synthetic approach. First, SiO_2 NPs were obtained with the typical Stöber approach, which served as core for TiO_2 deposition resulting in the growth of SiO_2–TiO_2 core–shell (ST CS) NPs. After modified by polyvinylpyrrolidone (PVP), additional SiO_2 layer can be coated on the TiO_2 surface of ST CS NPs in a sol–gel reaction.
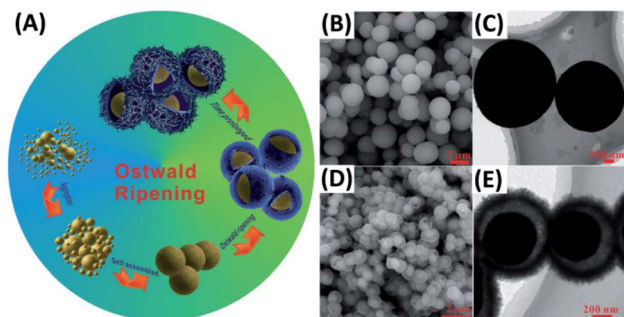

Fig. 3 (A) Synthetic approach to N-doped TiO_2–C yolk–shell spheres by Ostwald ripening. (B and C) SEM and TEM images for solid TiO_2. (D and E) SEM and TEM images for N-doped TiO_2–C. Reproduced with permission from ref. 72. Copyright 2016, Wiley.
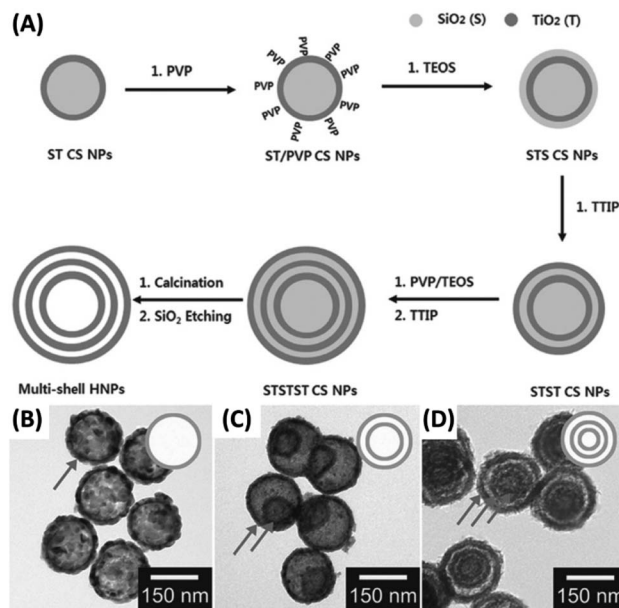

Fig. 4 (A) Synthetic approach to multi-shell TiO_2 hollow NPs by chemical etching. (B–D) TEM images for (B) single-shell, (C) double-shell and (D) multi-shell TiO_2. Reproduced with permission from ref. 77. Copyright 2014, Wiley.

Further TiO_2 deposition can be achieved, leading to the formation of SiO_2–TiO_2–SiO_2–TiO_2 (STST) CS NPs. Repeated procedures can be employed to produce STSTST CS NPs, which were then calcinated and etched with NaOH to create multi-shell TiO_2 hollow NPs. Fig. 4B–D show TEM images of the single-shell, double-shell, and multi-shell TiO_2 hollow NPs. These NPs all possessed an overall size of around 160 nm and a shell thickness of 15 nm. Additional structural feature worth noting was that the inner shell did not constantly lie at the middle of outer shell. This observation implied that the inner shell can freely move within the outer shell, a conspicuous feature for yolk–shell nanostructures. As a template-assisted approach, chemical etching can serve as a versatile platform for the synthesis of yolk–shell nanostructures. The remaining issue is the durability of the components during the template removal process because strong acids/bases are usually used.

2.5 Thermal treatment

Another versatile manner to manufacture yolk–shell nanostructures is to decompose and remove the volatile components under high temperature. Yolk–shell nanostructures with a variety of compositions can be created by using such a thermal treatment method. The examples include $MnFe_2O_4$–SnO_2,[78] C–N-doped $ZnFe_2O_4$,[79] Fe–FeN_x,[80] C–TiO_2[81] and Fe_2O_3.[82] Son et al. successfully synthesize Fe_2O_3 yolk–shell particles through multiple-step spray pyrolysis.[82] Fig. 5A illustrates the one-pot synthetic process for the products. The sucrose-containing droplets of Fe nitrate were first generated by ultrasonic nebulization. Upon air-drying, decomposition, polymerization and carbonization, C–Fe_2O_3 composite particles were obtained. Further combustion and contraction in thermal treatment gave
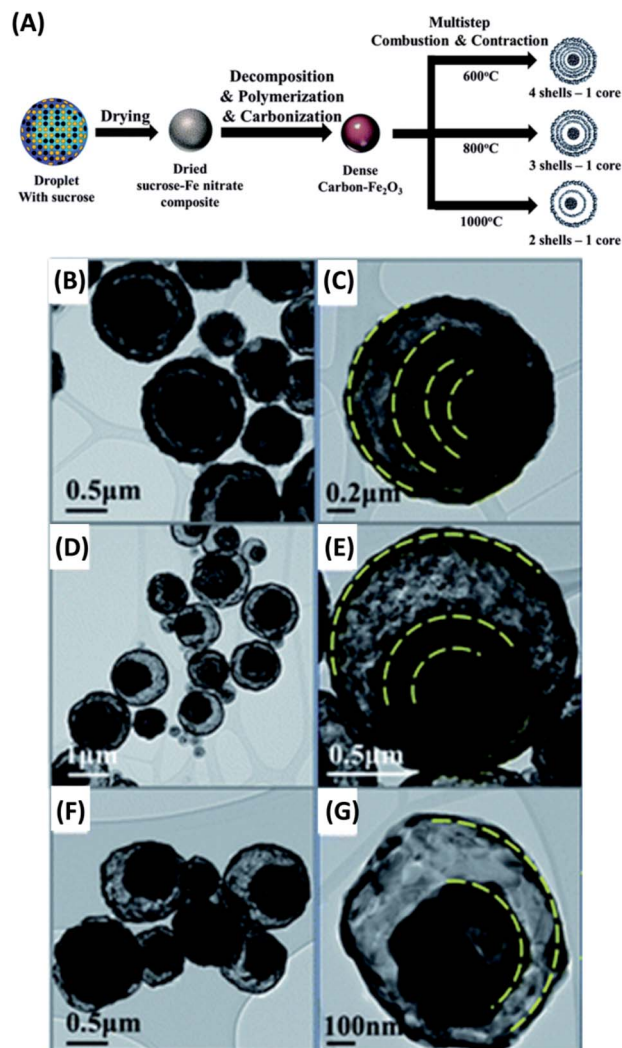
Fig. 5 (A) Synthetic approach to Fe_2O_3 yolk–shell particles by thermal treatment. (B–G) TEM images for Fe_2O_3 yolk–shell particles with (B and C) four, (D and E) three, and (F and G) two shells. Reproduced with permission from ref. 82. Copyright 2013, Royal Society of Chemistry.

rise to Fe_2O_3 yolk–shell particles. Interestingly, the shell number of the resultant yolk–shell particles can be adjusted by tuning combustion rate and temperature. Slow combustion at low temperature (600 °C) produced Fe_2O_3 with four shells, while fast combustion at high temperature (800 °C or 1000 °C) generated Fe_2O_3 with three or two shells. Fig. 5B–G show the corresponding TEM images for the three samples, which all had a similar outer diameter. The thermal treatment approach is especially suited for the synthesis of metal oxides-based yolk–shell nanostructures since high-temperature operation is needed. Similar to the concern for chemical etching approach, particular attention should be taken on the possible deterioration of materials properties under the harsh high-temperature conditions.

3. Photocatalytic applications

3.1 Dye degradation

Photocatalysis has received much attention in remedying environmental problems in the past two decades. Such a pollution abatement method is especially effective for treating dyeing wastewater. The working mechanism relies on the strong oxidizing power of charge carriers produced by photocatalysts, which can completely oxidize and decompose dye molecules. Heretofore, a multitude of works have demonstrated the use of yolk–shell nanostructures for dye degradation with the aim to treat dyeing wastewater. The reported photocatalysts include $Ag/TiO_2–SiO_2$,[83] $Si/SiC–C/TiO_2$,[84] $Au–CeO_2$,[85] and Ag/TiO_2.[86]

Zhao *et al.* demonstrated the preparation of $Ag/TiO_2–SiO_2$ yolk–shell nanostructures with tunable void size by using chemical etching and thermal treatment approach.[83] This work demonstrated the practical use of $Ag/TiO_2–SiO_2$ as photocatalysts for methylene blue (MB) degradation. As illustrated in Fig. 6A, there were several advantages of using $Ag/TiO_2–SiO_2$: (1) Ag/TiO_2 yolk can function as visible photocatalyst due to the plasmonic effect of Ag; (2) tunable void size offered feasibility of optimizing photocatalytic activity; (3) porous SiO_2 shell enabled light penetration and diffusion of reactive species; (4) protective function of euphotic SiO_2 made possible the preservation of polymer supports (*e.g.* textile and cloth) for better versatility. Fig. 6B and C display SEM and TEM images for $Ag/TiO_2–SiO_2$, showing a mean overall size of 190–220 nm and recognizable porosity at SiO_2 shell. Fig. 6D illustrates the optimization of photocatalytic performance of $Ag/TiO_2–SiO_2$ by controlling the void size. Here, the control over void size was realized by tuning the thickness of the sacrificial polyporrole (PPy) layer. The samples prepared with the removal of one and three PPy layers had limited void space for efficient MB degradation, whereas the sample obtained by removing seven PPY layers had opening
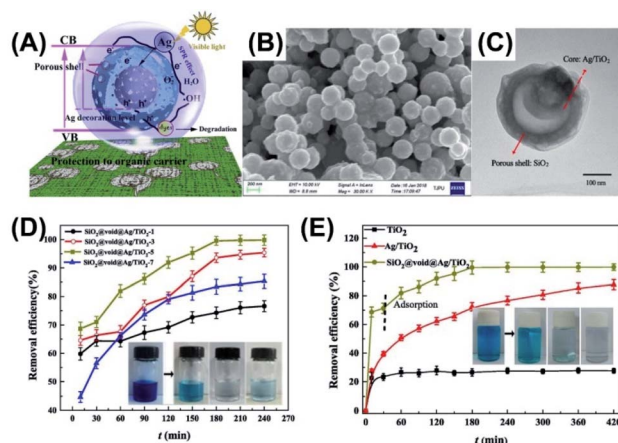
Fig. 6 (A) Plausible charge transfer mechanism for superior photocatalytic efficiency of $Ag/TiO_2–SiO_2$ toward MB degradation, (B and C) SEM and TEM images of $Ag/TiO_2–SiO_2$, (D) photocatalytic performance of $Ag/TiO_2–SiO_2$ prepared with the removal of different Ppy layers, (E) comparative results of MB degradation under visible light illumination. Reproduced with permission from ref. 83. Copyright 2019, Elsevier.

voids that can break the structural integrity. As a result, Ag/TiO$_2$–SiO$_2$ prepared with the removal of five PPy layers displayed the best performance toward MB degradation. Fig. 6E further compares the photocatalytic performance of Ag/TiO$_2$–SiO$_2$ with pure TiO$_2$ and pristine Ag/TiO$_2$. A superior MB degradation efficiency was observed for Ag/TiO$_2$–SiO$_2$ in terms of better adsorption capacity and higher photocatalytic activity, which can be attributed to the synergistic effect illustrated in Fig. 6A. The as-synthesized Ag/TiO$_2$–SiO$_2$ was further loaded on cotton textiles to demonstrate the scenario of practice use. Comparative results showed that after two days of irradiation pristine Ag/TiO$_2$-loaded textiles were inclined to structural collapse, while Ag/TiO$_2$–SiO$_2$-loaded textiles were structurally unscathed. This work offered an effective approach to the development of textile-supported photocatalysts with easy disposal and favorable recovery. The superior photocatalytic efficiency of yolk–shell nanostructures toward dye degradation can be recognized from the comparison of apparent rate constant of dye degradation. In a typical example,[87] yolk–shell spheres of TiO$_2$ were prepared and utilized for photodegradation of rhodamine B. The achieved pseudo-first-order rate constant of yolk–shell TiO$_2$ spheres was 0.0057 min^{-1}, almost four times the value of commercial TiO$_2$ powders (P25) (0.0015 min^{-1}).

3.2 Toxics decomposition

As the modern chemical industries prosperously develop, toxic organic compounds, such as chlorinated and polycyclic aromatic hydrocarbons, have become global environmental pollution. Among various organic toxics, 2,4-dichlorophenol (2,4-DCP) is considered as a particularly dangerous pollutant worldwide because of its wide use as sanitizer and yet the potential lethality.[88] Therefore, developing effective means to decomposing 2,4-DCP are highly required. Photocatalysis using semiconductor nanostructures is regarded as a reliable and green technique to achieve decomposition of toxic organic compounds.[89,90] Previous studies have demonstrated many efficient photocatalytic systems capable of decomposing toxic substances based on the use of yolk–shell nanostructures like LaFeO$_3$,[91] Mn$_2$O$_3$–Mn$_5$O$_8$,[92] and NiFe$_2$O$_4$–C.[93]

In a study led by Khan *et al.*,[91] a delicate thermal treatment-based method was developed to prepare for yolk–shell LaFeO$_3$ (YS-LFO) microspheres by using carbon microspheres as template. To further enhance the photocatalytic activity, YS-LFO was coupled with SnO$_2$ particles to enhance charge separation. As displayed in Fig. 7A, SnO$_2$ can function as photoelectron modulator to receive high-level photoexcited electrons from LFO, prohibiting their relaxation to the bottom of CB. This would largely reduce charge recombination to allow the localized holes for conducting decomposition of 2,4-DCP. Fig. 7B–D clearly show the ball-in-sphere, yolk–shell structure for YS-LFO and its successful coupling with SnO$_2$. For YS-LFO, the solid yolk had a diameter of 200–300 nm, and the whole sphere had an outer diameter of around 1 μm. The coupled SnO$_2$ particles had a diameter of 20 nm and were evenly distributed at the surface of YS-LFO. Fig. 7E and F compare the photocatalytic performance of 2,4-DCP decomposition among different
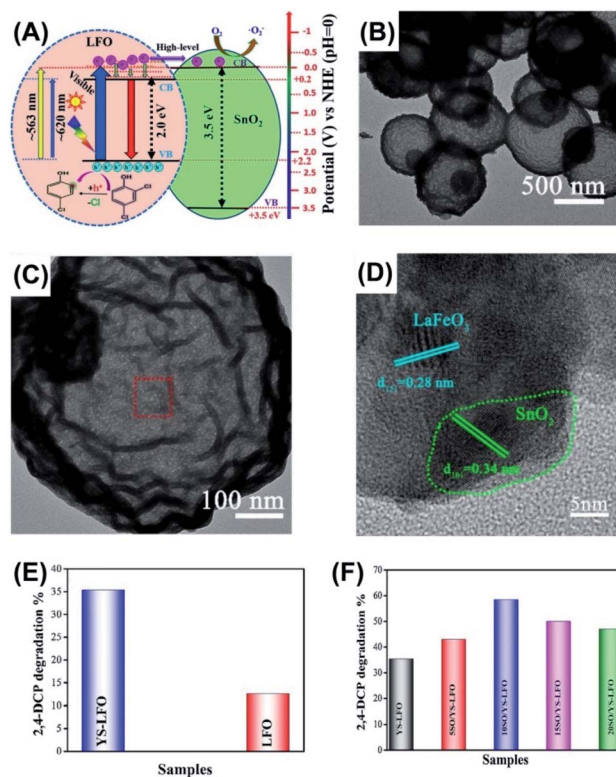

Fig. 7 (A) Plausible charge transfer mechanism for YS-LFO coupled with SnO$_2$, (B) TEM image of YS-LFO, (C and D) TEM images of SnO$_2$-coupled YS-LFO, (E and F) comparative results of 2,4-DCP decomposition under visible light illumination. Reproduced with permission from ref. 91. Copyright 2020, Elsevier.

samples. Compared to pure LFO solid particles, YS-LFO exhibited better photocatalytic efficiency. This could be attributable to the increase of surface area and the improvement in photon harvesting endowed by the yolk–shell architecture. Significantly, after coupling with 10 wt% of SnO$_2$ (10SO/YS-LFO), the photocatalytic efficiency of YS-LFO can increase by 1.6 times, highlighting the beneficial function of SnO$_2$. The apparent rate constant can also serve as a direct index of evaluating photocatalytic activity of toxics decomposition for yolk–shell nanostructures. For example, Bi–SnO$_2$ yolk–shell photocatalysts showed a remarkable rate constant of tetracycline degradation (0.014 min^{-1}) relative to pure solid Bi (0.00072 min^{-1}).[76]

3.3 CO$_2$ reduction

The concentration of CO$_2$ in atmosphere has been increasing year by year due to the prosperous development of human society. This would cause greenhouse effect and global warming, which arouses general agreement for reducing CO$_2$ emission as well as consuming CO$_2$ on demand. Photocatalysis on semiconductor nanostructures is a potential manner of converting CO$_2$ into other high value-added hydrocarbon fuels, such as CH$_4$, C$_2$H$_6$ and CH$_3$OH. The goal of CO$_2$ reduction is imitating natural photosynthesis in order to balance the global CO$_2$ footprint. Many yolk–shell nanostructures have

demonstrated remarkable photocatalytic activity toward CO_2 reduction, including Au–TiO_2,[94] Au-g-C_3N_4/SnS,[95] Ni–SiO_2,[96] TiO_2,[97] and TiO_{2-x}.[98]

Ziarati et al. obtained a yolk–shell nanostructure of TiO_2 (Y@S–TiO_2) based on the Ostwald ripening approach in a solvothermal reaction.[98] After hydrogenation treatment, the TiO_{2-x} yolk–shell nanostructures (Y@S–TiO_{2-x}) were decorated with Co–Al layered double hydroxides (LDHs), producing Y@S–TiO_{2-x}/LDH core/shell nanospheres. Here, hydrogenation can create oxygen vacancies for TiO_2, which not only reduced bandgap of TiO_2, but also served as adsorption sites for CO_2. The decoration of Co–Al LDHs on the other hand can improve charge separation of TiO_{2-x}. The porous features of LDHs can also promote CO_2 adsorption. These attributes were all beneficial for increasing photocatalytic activity of CO_2 reduction. Fig. 8A and B clearly reveal the yolk–shell structural features for TiO_{2-x} and the successful decoration with Al–Co LDHs. Fig. 8C compares the results of photocatalytic CO_2 reduction among different samples in terms of CH_3OH production. Several important points can be observed. First, P25 were almost inactive due to the poor visible light absorption. Second, P25/LDH showed better photocatalytic activity than P25 and LDH did, highlighting the synergy of LDHs with TiO_2 for promoting the efficiency of CO_2 reduction. Third, hydrogenated TiO_2 showed much higher activity than non-treated TiO_2 (H–P25/LDH vs. P25/LDH and Y@S–TiO_{2-x}/LDH vs. Y@S–TiO_2/LDH). This revealed the importance of hydrogenation treatment for promoting CO_2 reduction activity of TiO_2. Compared with P25 and LDH, a 20-fold increase in CH_3OH production can be achieved on Y@S–TiO_{2-x}/LDH. Such a superior performance can be realized by the attributes associated with structural engineering and charge transfer as illustrated in Fig. 8D. It is interesting to note that CH_3OH was the main product at the first

2 h of photocatalytic reaction. Further extending the reaction time led to the gradual production of CH_4 in addition to CH_3OH. This finding illustrated that the selectivity of CO_2 reduction on Y@S–TiO_{2-x}/LDH could be adjusted by controlling the reaction time. It should be noted that photocatalytic CO_2 reduction on yolk–shell nanostructures is at the infant stage, making it difficult to assess the actual performance. Quantitative indexes, e.g. apparent quantum yield (AQY) and solar-to-fuel conversion efficiency, enabling the reliable evaluation and global comparison of CO_2 reduction activity for different yolk–shell nanostructure systems are indispensable.

3.4 H_2 production

H_2 production on semiconductor photocatalysts from water splitting represents a viable, green approach to creation of alternative energy. Ever since Fujishima and Honda demonstrated water photolysis on TiO_2 photoelectrodes,[99] photocatalytic H_2 production has been an ultimate goal of solar energy conversion in the search for clean energy. There are many strategies developed to enhance the efficiency of solar H_2 production. Employing unique nanostructures to better harvest solar energy is particularly important because light absorption is the leading process determining how many charge carriers can be produced. In this regard, yolk–shell nanostructures offer an ideal structural platform since light harvesting efficiency can be enhanced as a result of multi-reflection of incident light within the void space. Till now, a variety of yolk–shell nanostructures have demonstrated remarkable activity of photocatalytic H_2 production, such as Au–TiO_2[100,101] and Au–CdS.[63,102]

Shi et al. prepared for Au–TiO_2 yolk–shell nanospheres with a chemical etching method.[100] These nanospheres were assembled into three-dimensional arrays (3D-array) to study the multi-scattering effect on the photocatalytic activity of H_2 production. Fig. 9A depicts the charge transfer mechanism for Au–TiO_2. The plasmonic Au yolk can be excited by visible light, generating hot electrons for enhancing the photoactivity of TiO_2. As Fig. 9B shows, the as-prepared Au–TiO_2 was highly
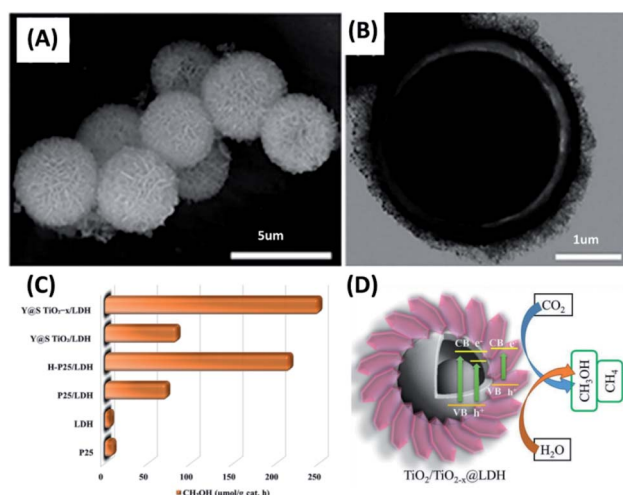
Fig. 8 (A and B) SEM and TEM images of Y@S– TiO_{2-x}/LDH. (C) Comparative results of CO_2 reduction in terms of CH_3OH production under visible light illumination. (D) Plausible charge transfer mechanism for superior photocatalytic efficiency of Y@S–TiO_{2-x}/LDH toward CO_2 reduction. Reproduced with permission from ref. 98. Copyright 2019, American Chemical Society.
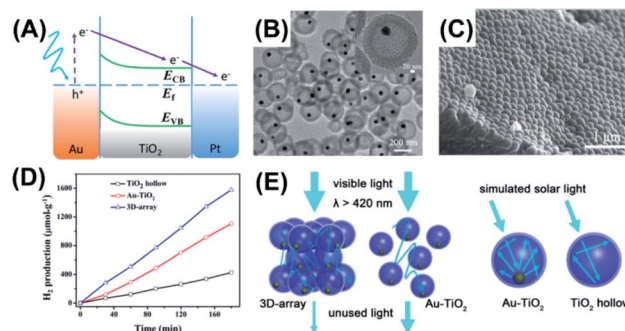
Fig. 9 (A) Plausible charge transfer mechanism for superior photocatalytic efficiency of Au–TiO_2 toward H_2 production, (B) TEM image of Au–TiO_2, (C) SEM image of 3D-array, (D) comparative results of H_2 production under simulated daylight illumination, (E) schematic illustration of multi-scattering effect and increased light reflection for 3D-array and Au–TiO_2. Reproduced with permission from ref. 100. Copyright 2016, ACS publications.

mono-dispersed with a uniform shell thickness of 46 nm and inner cavity size of 176 nm. The SEM image in Fig. 9C clearly reveals the orderly packed, hexagonal structure for 3D-array. These arrays comprised several layers of Au–TiO$_2$, which may facilitate light scattering between the individual Au–TiO$_2$ spheres. Fig. 9D compares the photocatalytic activity of H$_2$ production among three relevant samples. Compared with hollow TiO$_2$, both 3D-array and non-assembled Au–TiO$_2$ showed much higher activity of H$_2$ production, manifesting the beneficial function of the plasmonic Au. Significantly, 3D-array showed 1.4 folds higher activity than non-assembled Au–TiO$_2$. As Fig. 9E illustrates, the superior activity of 3D-array can be attributed to the improved photon harvesting resulting from the multi-scattering of incident light between the individual Au–TiO$_2$. On the other hand, photon harvesting can also be augmented in each of the yolk–shell particles because incident light can be reflected many times within the void space. As a result of the increased light refection inside the TiO$_2$ shell, the plasmonic Au yolk can generate more hot electrons for improving the photocatalytic activity. The superior photo-catalytic performance of yolk–shell nanostructures toward H$_2$ production can be reflected from the unprecedented AQY value. In Chiu's work,[63] Au–CdS yolk–shell nanostructures achieved an AQY value of 4.22% at 420 nm without the use of Pt co-catalysts. This value was substantially larger than that of Pt-deposited Au–CdS core–shell nanostructures (1.9%),[103] highlighting the great promise of yolk–shell nanostructures for photocatalytic H$_2$ production.

3.5 O$_2$ production

Compared to H$_2$ production, there are relatively few kinds of photocatalysts that exhibit valid activity of O$_2$ production from water splitting. The cause is the higher kinetics difficulty of water oxidation, which requires four equivalent holes in order to produce an O$_2$ molecule. Despite the difficulty, O$_2$ production is still an important reaction with regard to the realization of overall water splitting. The use of yolk–shell nanostructures for conducting photocatalytic O$_2$ production is quite limited. The successful example was demonstrated on Fe$_2$TiO$_5$–TiO$_2$.[104]

Among the different semiconductor photocatalysts, TiO$_2$ and α-Fe$_2$O$_3$ are particularly suited for conducting photocatalytic O$_2$ production by virtue of the sufficiently anodic VB level (E_{VB} = +2.91 eV vs. NHE for TiO$_2$; E_{VB} = +2.48 eV vs. NHE for α-Fe$_2$O$_3$). Waqas et al. prepared for Fe$_2$TiO$_5$–TiO$_2$ yolk–shell hollow spheres (FTYS-HS) with a thermal treatment method and demonstrated effective photocatalytic O$_2$ production.[104] Here, Fe$_2$TiO$_5$ has a band structure straddling that of TiO$_2$ and α-Fe$_2$O$_3$. By combining Fe$_2$TiO$_5$ with TiO$_2$, the photocatalytic O$_2$ production efficiency can be enhanced as a result of the improved charge transfer.[105] Fig. 10A shows the high-angle annular dark-field (HAADF) scanning TEM image and the cor-responding energy-dispersive spectrometry (EDS) mapping data for FTYS-HS, which revealed uniform distribution of Ti and Fe at the yolk and shell regions. Fig. 10B compares the photo-catalytic activity of O$_2$ production among four relevant samples. As expected, FTYS-HS achieved a much higher activity of O$_2$
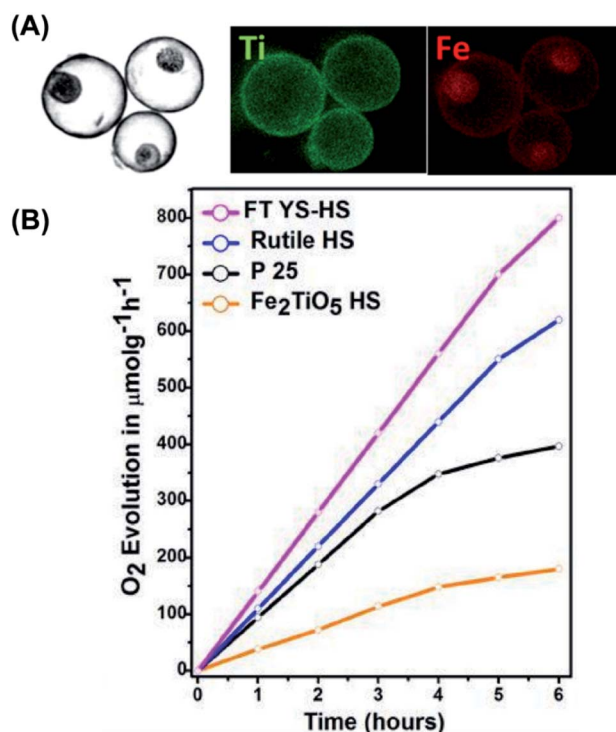

Fig. 10 (A) HAADF scanning TEM image and the corresponding EDS data of FTYS-HS, (B) comparative results of O$_2$ production under white light illumination. Reproduced with permission from ref. 104. Copy-right 2017, Elsevier.

production than P25, rutile TiO$_2$ hollow spheres (rutile HS), and Fe$_2$TiO$_5$ hollow spheres (Fe$_2$TiO$_5$ HS). The superiority of FTYS-HS can be partly assigned to Fe$_2$TiO$_5$/TiO$_2$ heterojunction which improved charge carrier separation.[106] The multi-reflection of incident light inside the yolk–shell structures contributed to the enhanced photocatalytic activity of FTYS-HS as well. Similar to the case of CO$_2$ reduction, only a limited number of examples have demonstrated the practice of yolk–shell nanostructures in photocatalytic O$_2$ production. Future effort can be focused on the survey of more yolk–shell nano-structures candidates to construct photocatalytic systems for efficient O$_2$ production.

3.6 Fine chemicals synthesis

Fine chemicals synthesis by means of photocatalytic redox reactions is a prosperous topic attracting interdisciplinary scientists. Traditionally, fine chemicals are manufactured under harsh conditions, such as high temperature and highly oxidative environment. Although high yield with a good selec-tivity can be achieved, the traditional approach is costly and harmful, and therefore, is not viable from the economic and environmental points of view. As an alternate, using photo-catalysts to synthesize fine chemicals has received increasing attention. Examples include the production of aldehydes by photocatalytic oxidation[107–110] and the generation of amines by photocatalytic reduction.[111–114] Yolk–shell nanostructures have

also demonstrated remarkable photocatalytic activity for synthesis of fine chemicals.[115–120]

In a study by Ziarati et al., yolk–shell TiO$_2$ structures (Y@S–TiO$_2$) were prepared in a solvothermal reaction via Ostwald ripening.[118] The obtained Y@S–TiO$_2$ was further modified with di-amines to wrap graphene sheets in a high level. The resultant graphene highly wrapped yolk–shell TiO$_2$ (G-HW-Y@S–TiO$_2$) architectures showed good selectivity of producing aldehydes in the photocatalytic oxidation of aromatic alcohols. Fig. 11A–C show the SEM and TEM images for G-HW-Y@S–TiO$_2$. Successful wrapping of 5 nm-thick graphene sheets can be recognized. In Fig. 11D, the photocatalytic efficiency of G-HW-Y@S–TiO$_2$ toward selective oxidation of benzyl alcohol was investigated and compared with other counterpart samples, including graphene wrapped TiO$_2$ (G-W-TiO$_2$), graphene wrapped hollow TiO$_2$ (G-W-H-TiO$_2$) and graphene lightly wrapped yolk–shell TiO$_2$ (G-W-Y@S–TiO$_2$). G-W-TiO$_2$ showed mediocre activity with a moderate conversion rate (47%) and benzaldehyde selectivity (61%). For G-W-H-TiO$_2$, the conversion rate (78%) and

selectivity (94%) can be largely increased. Significantly, G-W-Y@S–TiO$_2$ and G-HW-Y@S–TiO$_2$ showed nearly 100% of benzaldehyde selectivity, with G-HW-Y@S–TiO$_2$ exhibiting a little bit higher conversion. The superior performance of G-HW-Y@S–TiO$_2$ for selective oxidation of benzyl alcohol can be attributed to the synergy among several factors. Note that graphene had a work function (4.42 eV) larger than TiO$_2$ (4.21 eV).[121] The photoexcited electrons of TiO$_2$ were then transferred to graphene, leaving photoexcited holes at TiO$_2$. Therefore, the photocatalytic oxidation reaction mostly occurred at the TiO$_2$ surface of G-HW-Y@S–TiO$_2$. As illustrated in Fig. 11E, the hydrophilic alcohol reactant first diffused through the mesoporous shell, reacted with the photoexcited holes at TiO$_2$ yolk, and produced benzyl alcohol cation radicals. At the same time, the photoexcited electrons at graphene reacted with the dissolved O$_2$ and generated ˙O$_2^-$. The cation radicals further reacted with ˙O$_2^-$ and produced benzaldehydes. Such a partially oxidized product was hydrophobic, which can be repulsed by the hydrophilic surface of TiO$_2$ and would thus diffuse outward prior to further oxidation. The wrapped graphene sheets on the other hand can prevent the effluent benzaldehydes from direct contact with TiO$_2$, prohibiting them from being oxidized by the photoexcited holes at TiO$_2$. This explained why such a high selectivity can be achieved on G-HW-Y@S–TiO$_2$.

Since the pioneering work published by Akira Suzuki in 1979,[122] Suzuki–Miyaura coupling reaction has been widely utilized to synthesize a variety of technologically important organic molecules, such as styrenes and biphenyls. Typical Suzuki–Miyaura coupling reactions use Pd as catalysts. Photocatalysts containing Pd are also capable of conducting efficient coupling reactions[119,123–125] In the study by Rohani et al.,[128] yolk–shell structures comprising hydrogenated urchin-like TiO$_2$ shell and TiO$_2$ yolk (HUY@S-TOH) were prepared in an Ostwald ripening-based dissolution–recrystallization process. These yolk–shell structures were decorated with Au–Pd core–shell particles (HUY@S-TOH/AuPd), which were employed as photocatalysts to carry out Suzuki–Miyaura coupling reaction. In Fig. 12A and B, the TEM images clearly revealed the yolk–shell feature of HUY@S-TOH and the successful decoration of 5 nm-sized Au/Pd particles. The photocatalytic efficiency was studied by carrying out coupling reaction of 4-iodotoluene with phenylboronic acid under visible light illumination. The expected product was biphenyls. Four relevant samples, including P25 TiO$_2$, P25/AuPd, Y@S-TO/AuPd, HUY@S-TOH/Au, HUY@S-TOH/Pd and HUY@S-TOH/AuPd, were tested and compared. Notably, P25 TiO$_2$ showed negligible activity, while P25/AuPd was significantly active. This finding pointed out the necessity of using Au/Pd particles to conduct Suzuki–Miyaura coupling reaction. On the other hand, because of the higher surface area and enhanced photon harvesting inside the yolk–shell structures, Y@S-TO/AuPd showed much higher activity than P25/AuPd did. Among the different samples, HUY@S-TOH/AuPd showed the best activity in terms of biphenyls yield with a turnover frequency (TOF) of 7095 h^{-1}. As summarized in Fig. 12C, this TOF value was considerably higher than the performance of the state-of-the-art photocatalysts ever reported. Fig. 12D further depicts the charge transfer mechanism
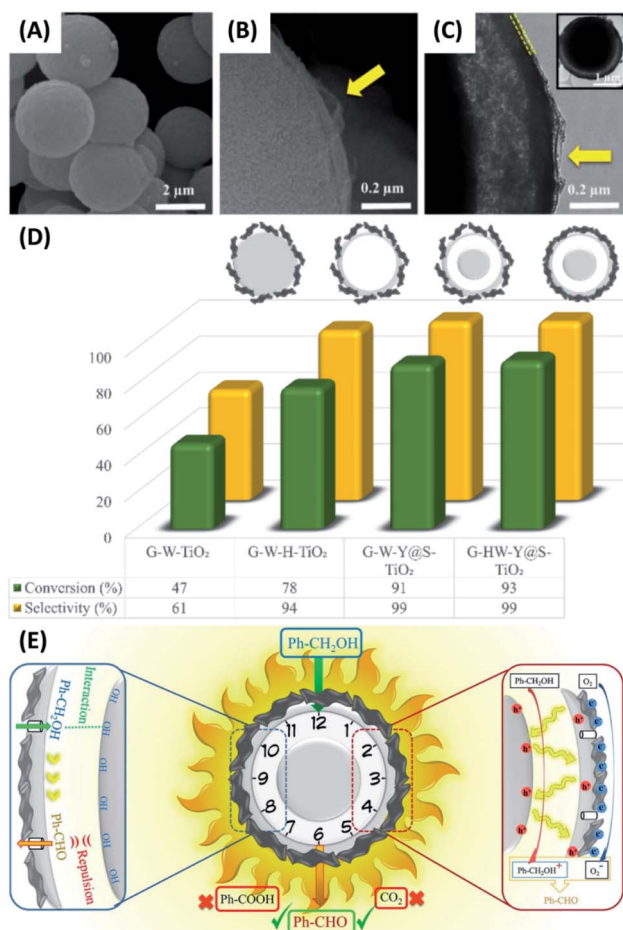

Fig. 11 (A–C) SEM and TEM images of G-HW-Y@S–TiO$_2$. (D) Comparative results of selective benzyl alcohol oxidation under visible light illumination. (E) Plausible charge transfer mechanism for superior photocatalytic activity of G-HW-Y@S–TiO$_2$ toward selective benzyl alcohol oxidation. Reproduced with permission from ref. 118. Copyright 2018, Elsevier.
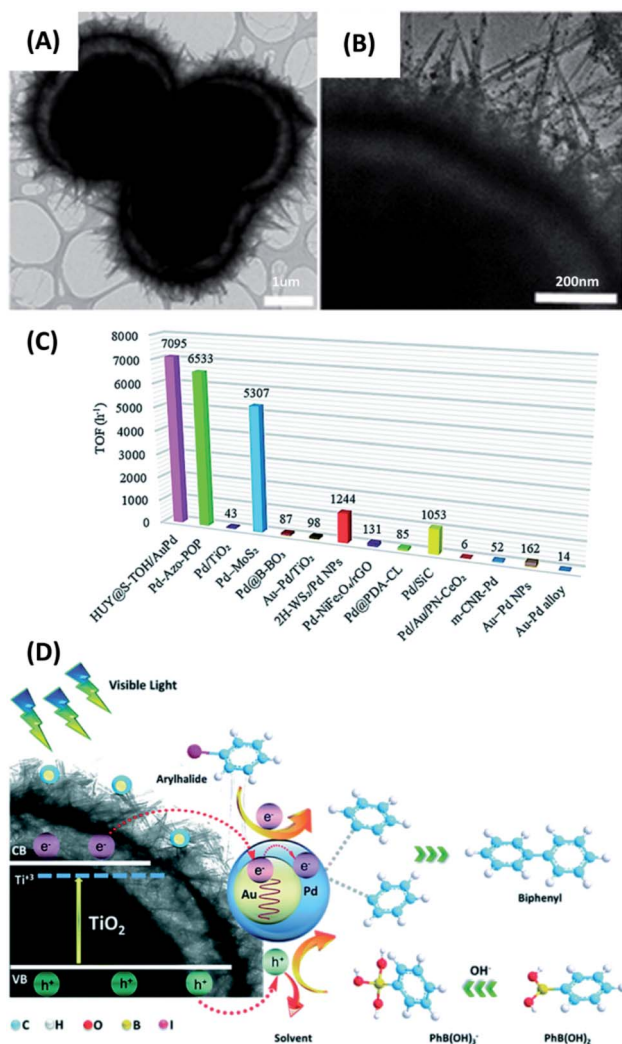
Fig. 12 (A and B) TEM images of HUY@S-TOH/AuPd. (C) Comparison of TOF value with those achieved by state-of-the-art photocatalysts reported in the literature. (D) Plausible charge transfer mechanism for superior photocatalytic activity of HUY@S-TOH/AuPd toward Suzuki–Miyaura coupling reaction. Reproduced with permission from ref. 119. Copyright 2019, Royal Society of Chemistry.

accountable for the superior activity of HUY@S-TOH/AuPd. Hydrogenated TiO_2 was capable of harvesting visible photons to equip TiO_2 with visible photoactivity. Upon visible irradiation, the photoexcited electrons of hydrogenated TiO_2 may transfer to Au/Pd; meanwhile, hot electrons induced by plasmonic absorption of Au were injected to Pd. The C–X bonding of aryl halides can then be activated by the electron-enriched Pd, facilitating oxidative addition process of Suzuki reaction.[126] In the meantime, phenylboronic acid could be oxidized by photoexcited holes. Cross-coupling reaction then took place as the oxidized phenylboronic acids encountered the activated aryl halides, producing the expected product.

4. Interfacial charge dynamics

The efficiency of semiconductor photocatalysts is dependent on intrinsic properties, including light absorption, carrier transfer and recombination, and kinetics of surface redox reactions. The capability of light absorption inherits from the optical properties of the chosen photocatalysts, which can be augmented by means of dopant introduction and materials combination. Charge dynamics at interface dictates charge transfer and carrier utilization, the two determinant processes involved in the photocatalytic reactions. Under light illumination, the photoexcited electrons and holes are transported from the bulk of the photocatalysts to the surface region for conducting redox reactions. These charge carriers are however inclined to be trapped and recombined before they can eventually reach surface region. This would jeopardize carrier utilization efficiency and decrease the photocatalytic performance, making interfacial charge dynamics the most critical factor determining the overall photocatalytic efficiency. An in-depth understanding of how photoexcited charge carriers can be transported, trapped and/or recombined will enable performance optimization of semiconductor photocatalysts. In particular, establishing correlations between interfacial charge dynamics and photocatalytic activity can offer empirical yet practicable knowledge for devising versatile nanostructures for superior photocatalytic applications.

Compared to the extensive studies of interfacial charge dynamics on composite nanostructures like particle-decorated nanostructures[19–21,23–29,31–40] and core–shell nanocrystals,[43,45–47] examples are relatively scarce for the topic of studying charge dynamics on yolk–shell nanostructures.[63,81,101,102,127,128] In this section, we introduce two representative studies that explored the correlations of interfacial charge dynamics with the photocatalytic performance of H_2 production on yolk–shell nanostructures (Au–CdS[63] and Au–TiO_2 [101]). In addition to realization of charge dynamics, manipulation of charge transfer behaviors is also imperative with regard to the regulation of photocatalytic reactions. For yolk–shell nanostructures, spatial separation of photoexcited electrons and holes at the yolk and shell region is possible since the yolk is inherently separated from the shell. The spatial separation of electrons and holes not only guarantees long-lived charge separation but also inhibits backward reactions, both of which are crucial for reinforcing the utility in photocatalytic reactions. This concept has not been realized on yolk–shell nanostructures, but it has been widely demonstrated on hollow nanostructures, a structurally analogous example to yolk–shell model. Additional focus on the strategies of achieving spatial separation of charge carriers for hollow nanostructures will be placed in this section with the aim to provide applicable guidelines to yolks-shell nanostructures.

4.1 Charge dynamics of Au–CdS

In Chiu's study,[63] transient absorption (TA) spectroscopy was utilized to explore charge transfer dynamics of Au–CdS nanostructures. A definite correlation of interfacial charge dynamics and photocatalytic efficiency with the void size of Au–CdS was

established. Note that TA is a powerful ultrafast laser spectroscopic technique used to monitor the electronic transition processes of photoexcited charge carriers within semiconductor nanostructures. By identifying the photophysics beyond the recorded TA spectra, the interfacial charge dynamics of the samples can be clearly interpreted.

Fig. 13A and B show the TA spectra for pure hollow CdS and Au–CdS-4 recorded by increasing delay times from −2 to 100 ps at the probe wavelength between 450 to 750 nm. For pure CdS, a narrow negative bleaching was notices at 475 nm, which can be ascribed to the typical ground state bleaching of charge carriers from the excited CdS. This transient bleaching was however red-shifted to 515 nm for Au–CdS-4, reflecting pronounced electronic interaction between Au yolk and CdS shell. Most importantly, Au–CdS-4 showed much quicker decay of transient bleaching than pure CdS, suggesting the prevalence of additional electron transportation pathway from CdS to Au. Fig. 13C further compares the decay kinetics of TA bleaching for pure CdS and the four CdS–Au samples. Here, a counterpart sample by physically mixing pure CdS and Au NPs (denoted as CdS + Au) was also examined in order to highlight the superior feature of yolk–shell nanostructures. These TA profiles were fitted with a biexponential function to obtain the quantitative information of charge dynamics. Two lifetime components (τ_1 and τ_1) can be generated from the fitting, which was respectively associated with exciton decay processes induced by shallow and deep traps of CdS. To offer a global comparison, an intensity-weighted average lifetime, $<\tau>$, was presented, respectively giving 27.44 ps, 24.74 ps, 14.66 ps, 13.79 ps, 12.34 ps, and 11.71 ps for pure CdS, CdS + Au, Au–CdS-1, Au–CdS-2, Au–CdS-3, and Au–CdS-4. By considering that electron transportation from CdS to Au caused the reduced lifetime of Au–CdS, the rate constant of interfacial charge transfer (k_{ct}) can be obtained using the equation

$$k_{ct} \text{ (CdS} \rightarrow \text{Au)} = 1/<\tau> \text{ (Au–CdS)} - 1/<\tau> \text{ (pure CdS)}$$

The calculated k_{ct} value was respectively 0.40 × 10^{10} s^{-1}, 3.18 × 10^{10} s^{-1}, 3.61 × 10^{10} s^{-1}, 4.46 × 10^{10} s^{-1}, and 4.90 × 10^{10} s^{-1}
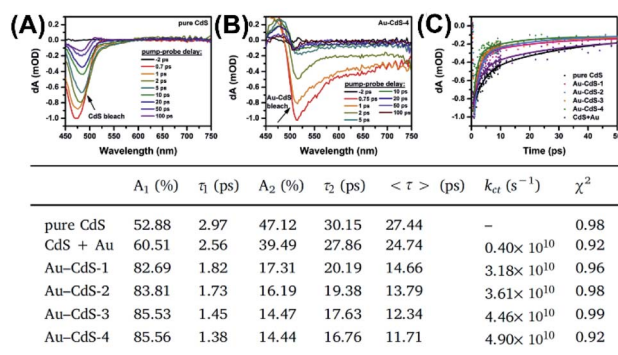
for CdS + Au, Au–CdS-1, Au–CdS-2, Au–CdS-3, and Au–CdS-4. There were two significant points to highlight. Firstly, compared to CdS + Au, the four Au–CdS samples all exhibited larger k_{ct}, signifying more efficient charge dynamics within the yolk–shell structure. Secondly, the k_{ct} of Au–CdS was enhanced as void size increased, suggesting that void size was a vital cause influencing charge transfer from CdS to Au. The implications of these two features in photocatalytic reactions were further explored. The comparative results of photocatalytic H$_2$ production showed consistency with the variation of k_{ct}, in which the four Au–CdS surpassed CdS + Au and CdS–Au-4 had the highest activity. This work highlighted the importance of understanding charge dynamics of yolk–shell nanostructures toward the optimization of photocatalytic performance.

4.2 Charge dynamics of Au–TiO$_2$

In Dillon's work,[101] Au–TiO$_2$ yolk–shell nanostructures with gradually improved shell crystallinity were prepared. The influence of shell crystallinity on the photophysics and its correlation with the resultant photocatalytic performance was investigated. In this study, time-resolved photoluminescence (PL) was employed to follow the dynamics of the photoexcited electrons and holes. Compared to TA, time-resolved PL offers a more intuitive viewpoint to explore the crystallinity effect on charge dynamics because PL emissions are highly sensitive to the crystallographic structure.[129–131]

Fig. 14A and B displays the time-resolved PL spectra recorded at 500 nm after 266 nm laser excitation at two time regimes (1 ns and 20 ns). Four Au–TiO$_2$ samples were compared, including the least crystalline sample A and the most crystalline sample D. Here, the emissions at 500 nm can be associated with charge recombination involving self-trapped excitons of TiO$_2$ or surface defects within TiO$_2$ lattice. The dynamics of this emission can thus reflect the degree of crystallinity of TiO$_2$. At both time regimes, sample D showed considerably slower PL decay

|	A$_1$ (%)	τ_1 (ps)	A$_2$ (%)	τ_2 (ps)	$<\tau>$ (ps)	k_{ct} (s^{-1})	χ^2
pure CdS	52.88	2.97	47.12	30.15	27.44	–	0.98
CdS + Au	60.51	2.56	39.49	27.86	24.74	0.40× 10^{10}	0.92
Au–CdS-1	82.69	1.82	17.31	20.19	14.66	3.18× 10^{10}	0.96
Au–CdS-2	83.81	1.73	16.19	19.38	13.79	3.61× 10^{10}	0.98
Au–CdS-3	85.53	1.45	14.47	17.63	12.34	4.46× 10^{10}	0.99
Au–CdS-4	85.56	1.38	14.44	16.76	11.71	4.90× 10^{10}	0.92

Fig. 13 (A and B) TA profiles of pure CdS and Au–CdS-4. (C) Kinetics of TA bleaching for relevant samples. Inserted table summarizes the fitting results. Reproduced with permission from ref. 63. Copyright 2019, Elsevier.
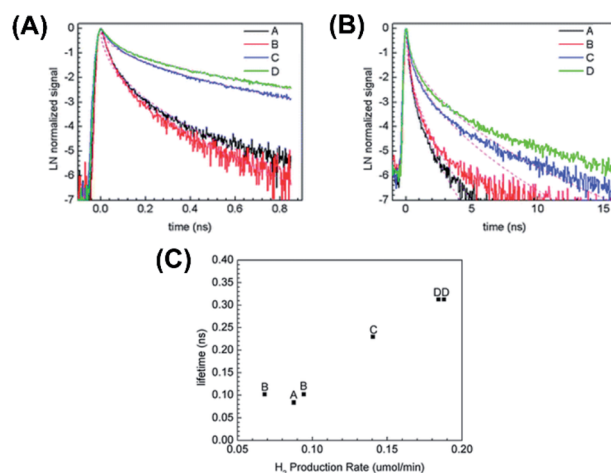

Fig. 14 (A and B) Time-resolved PL spectra of four Au–TiO$_2$ samples recorded at two time regimes. (C) Correlation of PL lifetime and H$_2$ production rate with the crystallinity of Au–TiO$_2$. Reproduced with permission from ref. 101. Copyright 2013, Royal Society of Chemistry.

kinetics than sample A did, suggesting that better crystallinity may lead to slower charge recombination as a result of the smaller number of defect sites. These kinetics profiles can be analyzed using a stretched exponential model, from which a characteristic lifetime was received. At 20 ns time regime, the computed lifetime of sample A, B, C, D was respectively 0.084 ns, 0.10 ns, 0.23 ns, 0.31 ns. The correspondence between charge dynamics and crystallinity degree was further correlated with the photocatalytic activity of H_2 production. In Fig. 14C, a clear correlation of PL lifetime with H_2 production rate was found. This correlation demonstrated that high degree of crystallinity was conducive to an enhanced photocatalytic activity for Au–TiO$_2$ as the number of defect sites may be reduced. This work also illustrated the promise of employing time-resolved PL to evaluate the photocatalytic performance of yolk–shell nanostructures.

4.3 Spatial separation of charge carriers

The concept of spatially separating photoexcited electrons and holes stems from the introduction of co-catalysts that have been widely employed to reduce the overpotentials of photocatalytic reactions. There are two types of co-catalysts used in photocatalysis; one functions as an electron trap site due to its large work function, such as Pt, Ag, Au particles (also known as reduction co-catalysts),[86,120,132,133] and the other one serves as a hole trap site, such as IrO_2, PbO_x, PbS, MnO_x, CoO_x (also known as oxidation co-catalysts).[120,133–138] The introduction of co-catalysts can anchor electrons or holes to guarantee long-lived charge separation.[120,123,125,133] Significantly, simultaneous loading of dual co-catalysts makes possible the spatial separation of electrons from holes, which can be utilized to achieve the concurrent occurrence of redox reactions at different sites. However, random deposition of dual co-catalysts may lead to the interference of redox reactions, arousing charge recombination and backward reactions to deteriorate the overall photocatalytic efficiency. Therefore, introducing dual co-catalysts at separate sites of photocatalysts is indispensable to achieving spatial separation of charge carriers.

The introduction of dual co-catalysts at separate sites has been realized on solid nanostructures with well-defined exposed facets, in which site-selective deposition of co-catalysts can be accomplished *via* photo-deposition.[133] For yolk–shell and hollow nanostructures which inherently have two separate sites, *i.e.* the inner and outer surfaces, selective deposition of dual co-catalysts at these surfaces can be more readily achieved. Domen's group demonstrated a successful practice of spatially selective deposition of dual co-catalysts on Ta_3N_5 hollow spheres, in which reduction (Pt) and oxidation (IrO_2) co-catalyst was respectively loaded at the inner and outer surface.[134] Upon light irradiation, the photoexcited electrons were attracted by Pt, while the photogenerated holes were trapped by IrO_2. As a result of the spatial separation of electrons and holes, charge recombination was greatly restrained, leading to a much enhanced photocatalytic activity of overall water splitting. In Zheng's work, hollow C_3N_4 structures were simultaneously deposited with Pt and Co_3O_4 co-catalysts to

demonstrate the effectiveness of photocatalytic overall water splitting.[138] The spatial separation of Pt (at inner surface of C_3N_4) from Co_3O_4 (at outer surface of C_3N_4) not only improved charge separation, but also inhibited the further reduction of O_2 at Pt. As Fig. 15 compares, a stoichiometric ratio of the produced H_2 to O_2 can be attained as Pt and Co_3O_4 were separately loaded on C_3N_4. If Pt and Co_3O_4 were both deposited at the outer surface of C_3N_4, a decrease in overall water slitting activity accompanied by reduced O_2 production otherwise resulted.

It should be noted that the dispersion and size of the loaded co-catalysts pose significant effect on the photocatalytic efficiency. Poor dispersion and uneven size distribution of co-catalysts can cause significant particle aggregation, reducing long-term stability to deteriorate the practice of photocatalysis. Devising a versatile synthetic procedure capable of depositing co-catalysts with good dispersion and uniform size is important to ensure the sustainable operation of photocatalysts. For yolk–shell and hollow nanostructures, it is difficult to control the dispersion and size of the deposited co-catalysts at inner surface, especially when the initial template or the resulting shell contains irregular porosity.[139] She *et al.*[137] and Sun *et al.*[139] employed zeolites with ordered micropores as a structurally confined template to allow for the loading of well-dispersed co-catalysts at the inner surface of hollow nanostructures. As displayed in Fig. 16, the nanoconfinement effect of zeolites enabled a fine tunability of dispersion, size and amount for the loaded MO_x (M = Pd, Co, Ni or Cu).[137] Further external growth of TiO_2 followed by the removal of zeolites resulted in the formation of TiO_2 hollow nanostructures with MO_x exactly deposited at the inner surface. The outer photo-deposited Pt can then be divided from the inner MnO_x by TiO_2, achieving great spatial separation for the dual co-catalysts to show remarkable
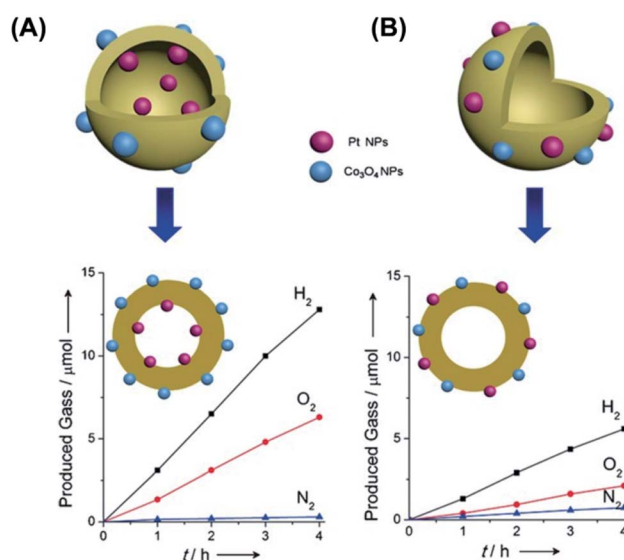

Fig. 15 Comparative results of photocatalytic water splitting under UV illumination on C_3N_4 hollow structures with (A) spatially separate co-catalysts and (B) randomly distributed co-catalysts. Reproduced with permission from ref. 138. Copyright 2016, Wiley.
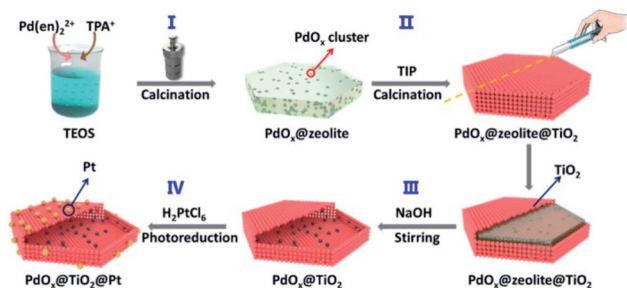
Fig. 16 Schematic illustration of using zeolites as structurally confined template to achieve spatial separation of dual co-catalysts on TiO_2. Reproduced with permission from ref. 137. Copyright 2020, American Chemical Society.

photocatalytic activity. On the other hand, atomic layer deposition (ALD) also offers feasibility for deposition of highly-dispersed co-catalysts at the selected positions. Zhang *et al.* employed ALD to sequentially deposit Pt nanoclusters and TiO_2 layer on carbon nanocoil (CNC) template.[135] Upon a removal of CNC, porous TiO_2 nanotubes with Pt deposited at the inner surface were obtained. Further ALD deposition of CoO_x produced TiO_2 nanotubes with Pt and CoO_x respectively loaded at the inner and outer surfaces. The amount and location of the loaded Pt and CoO_x can be finely controlled by adjusting ALD conditions, proven to be crucial for interfacial charge dynamics and determinant to the resultant photocatalytic activity.

Despite extensive efforts, it has been pointed out that the spatially separated co-catalysts can only enhance charge separation at surface and are not efficient for promoting charge separation in bulk. To address this issue, Li *et al.* prepare for TiO_2/In_2O_3 mesoporous hollow spheres and selectively deposited Pt and MnO_x at the inner and outer surface.[140] As illustrated in Fig. 17A and B, the idea was to combine the advantages of TiO_2/In_2O_3 as thin heterojunction, and Pt and MnO_x as spatially separated co-catalysts. Here, the thin heterojunction (overall thickness = 20 nm) can promote effective charge separation in the whole bulk region as the nominal diffusion path of charge carriers is comparable to the heterojunction thickness. The separated charge carriers can then be transported in an opposite direction to the surface region, where the electrons and holes were respectively trapped by Pt and MnO_x. With this synergy, much enhanced photocatalytic activity of O_2 production can be attained. Such a regulation of charge separation in the bulk can be evidenced by studying charge dynamics of the samples as they were placed in an environment containing electron and hole scavengers. Under this situation, charge dynamics of the samples can be dictated by bulk recombination. The resultant time-resolved PL data suggested that bulk recombination was indeed prohibited by the introduction of thin heterojunction. Likewise, Wang *et al.* proposed a thin heterojunction based on TiO_2/CdS hollow spheres (overall thickness = 23 nm) and loaded Pt and Co_3O_4 at the inner and outer surface, respectively.[136] As Fig. 17C and D illustrates, the synergy of thin heterojunction and spatially separated co-
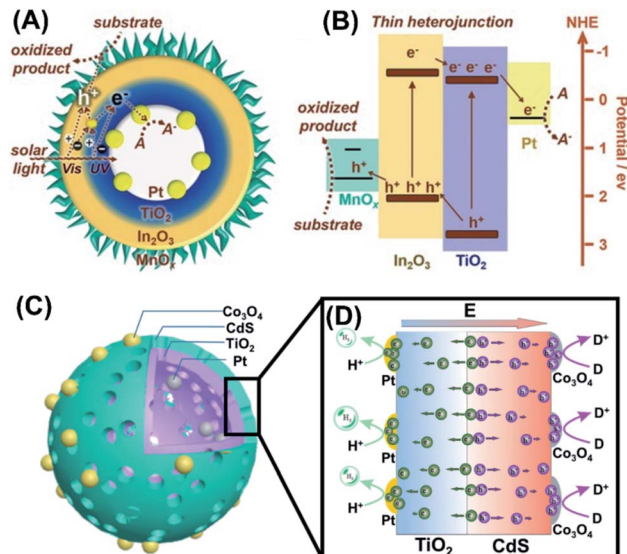

Fig. 17 (A) Microstructural model for TiO_2/In_2O_3 hollow spheres with Pt and MnO_x respectively deposited at the inner and outer surface. (B) Plausible charge transfer mechanism for superior photocatalytic activity of $Pt/TiO_2/In_2O_3/MnO_x$. Reproduced from ref. 140. Copyright 2016, Wiley. (C) Microstructural model for TiO_2/CdS hollow spheres with Pt and Co_3O_4 respectively deposited at the inner and outer surface. (D) Plausible charge transfer mechanism for superior photocatalytic activity of $Pt/TiO_2/In_2O_3/Co_3O_4$. Reproduced with permission from ref. 136. Copyright 2016, Wiley.

catalysts gave rise to a remarkable enhancement in the performance of solar H_2 production.

5. Conclusions and future perspective

In this review, the synthetic schemes for yolk–shell nanostructures are systematically organized. The formation of hollow shell can be attributed to the difference in solubility product for Kirkendall effect and the difference in redox potential for galvanic replacement. By pairing up materials with appropriate solubility products and redox potentials, yolk–shell nanostructures composed of various components can be readily obtained. Ostwald ripening takes the advantage of the dissolution-re-deposition principle during the process of crystal growth. The shell layer grows as the core particles dissolve, or the shell layer (or core particle) itself dissolves and re-crystallizes, both of which generate empty space between the core and shell as a result of the contraction of the dissolved components. Both chemical etching and thermal treatment are based on the assistance of sacrificial templates like SiO_2 and carbon. Upon a removal of the templates, cavity inside the shell can evolve. The necessity of removing templates by strong acids/bases or high-temperature calcination however poses significant concerns on whether or not the remaining components will be deteriorated in such a harsh condition. Definitely, yolk–shell nanostructures with tunable structural parameters are essential for further tailoring and optimizing the intrinsic

properties. Despite extensive synthetic efforts, it is difficult to achieve exact control over the size of void space and thickness of encircling shell because void formation and shell growth proceed simultaneously in most cases. Continuous efforts must be made to manipulate the growth of hollow shell and obtain yolk–shell nanostructures with controllable void size and shell thickness.

Compared to the structurally analogous counterpart, *i.e.* core–shell nanostructures, yolk–shell nanostructures have exceptional structural features that can be exploited to tailor the photocatalytic properties. For example, the movable yolk particles can stir the reaction solution inside the void space, creating a homogeneous reaction environment for accelerating mass transfer kinetics and thus enhancing the photocatalytic activity. An in-depth understanding of mass transfer kinetics across the shell can lay the foundation for constructing robust nanoreactors based on yolk–shell nanostructures. In terms of charge carrier transfer, a small number of studies are available on deriving the correlations of interfacial charge dynamics with the photocatalytic performance for yolk–shell nanostructures. The charge transfer between the yolk and the shell and its influence on the photocatalytic properties has seldom been examined. In particular, the movable yolk can cause ambiguous interpretation of charge transfer dynamics. Because the yolk particles are constantly moving during the photocatalytic process, complicated charge transfer and separation behaviors are expected. How to devise a realistic charge transfer mechanism by considering the influence of movable yolk is another focus of future direction. One future scenario of using yolk–shell nanostructures for advanced photocatalytic applications is spreading their powder into a polluted pond or river for environmental remediation. The empty space in the hollow shell enables yolk–shell nanostructures to float on water, providing high adaptability and recyclability for their participation in photocatalytic processes. On the other hand, spatial separation of photoexcited electrons and holes at the yolk and shell region is achievable for yolk–shell nanostructures. These separated charge carries can be more easily and separately accessible by the reactive species, allowing for the concurrent yet separate occurrence of reduction and oxidation reactions. This achievement is particularly appealing to overall water splitting and CO_2 reduction, the scenario of which can better operate as the redox reactions occur at different sites. It is thus not surprising to witness the realization of artificial photosynthesis by utilizing yolk–shell nanostructures. These demonstrations are not yet fully comprehended, requiring further efforts to make significant breakthrough.

Conflicts of interest

There are no conflicts to declare.

Acknowledgements

References

1 R.-B. Wei, Z.-L. Huang, G.-H. Gu, Z. Wang, L. X. Zeng, Y. B. Chen and Z.-Q. Liu, *Appl. Catal., B*, 2018, **231**, 101–107.

2 R. Shi, H.-F. Ye, F. Liang, Z. Wang, K. Li, Y. X. Weng, Z. S. Lin, W.-F. Fu, C.-M. Che and Y. Chen, *Adv. Mater.*, 2018, **30**, 1705941.

3 S. W. Cao, B. J. Shen, T. Tong, J. W. Fu and J. G. Yu, *Adv. Funct. Mater.*, 2018, **28**, 1800136.

4 S. B. Wang, B. Y. Guan and X. W. D. Lou, *J. Am. Chem. Soc.*, 2018, **140**, 5037–5040.

5 C. Y. Zhou, C. Lai, D. L. Huang, G. M. Zeng, C. Zhang, M. Cheng, L. Hu, J. Wan, W. P. Xiong, M. Wen, X. F. Wen and L. Qin, *Appl. Catal., B*, 2018, **220**, 202–210.

6 X.-J. Wen, C.-G. Niu, L. Zhang, C. Liang, H. Guo and G.-M. Zeng, *J. Catal.*, 2018, **358**, 141–154.

7 Q. Wang, W. Wang, L. L. Zhong, D. M. Liu, X. Z. Cao and F. Y. Cui, *Appl. Catal., B*, 2018, **220**, 290–302.

8 Y. Yang, Z. T. Zeng, C. Zhang, D. L. Huang, G. M. Zeng, R. Xiao, C. Lai, C. Y. Zhou, H. Guo, W. J. Xue, M. Cheng, W. J. Wang and J. J. Wang, *Chem. Eng. J.*, 2018, **349**, 808–821.

9 M. Barbero and S. Dughera, *Org. Biomol. Chem.*, 2018, **16**, 295–301.

10 S. Xu, P. Zhou, Z. Zhang, C. Yang, B. Zhang, K. Deng, S. Bottle and H. Zhu, *J. Am. Chem. Soc.*, 2017, **139**, 14775–14782.

11 W.-Y. Cheng, W.-T. Chen, Y.-J. Hsu and S.-Y. Lu, *J. Phys. Chem. C*, 2009, **113**(40), 17342–17346.

12 A. T. Nguyen, W.-H. Lin, Y.-H. Lu, Y.-D. Chiou and Y.-J. Hsu, *Appl. Catal., A*, 2014, **476**, 140–147.

13 Y.-H. Lu, W.-H. Lin, C.-Y. Yang, Y.-H. Chiu, Y.-C. Pu, M.-H. Lee, Y.-C. Tseng and Y.-J. Hsu, *Nanoscale*, 2014, **6**, 8796–8803.

14 Y.-H. Chiu, T.-H. Lai, C.-Y. Chen, P.-Y. Hsieh, K. Ozasa, M. Niinomi, K. Okada, T.-F. M. Chang, N. Matsushita, M. Sone and Y.-J. Hsu, *ACS Appl. Mater. Interfaces*, 2018, **10**(27), 22997–23008.

15 K.-A. Tsai, P.-Y. Hsieh, T.-H. Lai, C.-W. Tsao, H. Pan, Y.-G. Lin and Y.-J. Hsu, *ACS Appl. Energy Mater.*, 2020, **3**, 5322–5332.

16 P.-Y. Hsieh, T. Kameyama, T. Takiyama, K. Masuoka, T. Yamamoto, Y.-J. Hsu and T. Torimoto, *J. Mater. Chem. A*, 2020, **8**, 13142–13149.

17 Y.-C. Pu, Y.-C. Chen and Y.-J. Hsu, *Appl. Catal., B*, 2010, **97**, 389–397.

18 W.-T. Chen and Y.-J. Hsu, *Langmuir*, 2010, **26**, 5918–5925.

19 K.-H. Chen, Y.-C. Pu, K.-D. Chang, Y.-F. Liang, C.-M. Liu, J.-W. Yeh, H.-C. Shih and Y.-J. Hsu, *J. Phys. Chem. C*, 2012, **116**, 19039–19045.

20 Y.-C. Chen, Y.-C. Pu and Y.-J. Hsu, *J. Phys. Chem. C*, 2012, **116**, 2967–2975.

21 Y.-F. Lin and Y.-J. Hsu, *Appl. Catal., B*, 2013, **130–131**, 93–98.

22 Y.-C. Pu, G. Wang, K.-D. Chang, Y. Ling, Y.-K. Lin, B. C. Fitzmorris, C.-M. Liu, X. Lu, Y. Tong, J. Z. Zhang, Y.-J. Hsu and Y. Li, *Nano Lett.*, 2013, **13**, 3817–3823.

23 M.-Y. Chen and Y.-J. Hsu, *Nanoscale*, 2013, **5**, 363–368.

24 Y.-C. Chen, K.-I. Katsumata, Y.-H. Chiu, K. Okada, N. Matsushita and Y.-J. Hsu, *Appl. Catal., A*, 2015, **490**, 1–9.

25 K.-A. Tsai and Y.-J. Hsu, *Appl. Catal., B*, 2015, **164**, 271–278.

26 Y.-C. Pu, W.-H. Lin and Y.-J. Hsu, *Appl. Catal., B*, 2015, **163**, 343–351.

27 Y.-C. Chen, T.-C. Liu and Y.-J. Hsu, *ACS Appl. Mater. Interfaces*, 2015, **7**, 1616–1623.

28 Y.-H. Hsu, A. T. Nguyen, Y.-H. Chiu, J.-M. Li and Y.-J. Hsu, *Appl. Catal., B*, 2016, **185**, 133–140.

29 W.-H. Lin, Y.-H. Chiu, P.-W. Shao and Y.-J. Hsu, *ACS Appl. Mater. Interfaces*, 2016, **8**, 32754–32763.

30 T. H. Do, C. N. Van, K.-A. Tsai, L. T. Quynh, J.-W. Chen, Y.-C. Lin, Y.-C. Chen, W.-C. Chou, C.-L. Wu, Y.-J. Hsu and Y.-H. Chu, *Nano Energy*, 2016, **23**, 153–160.

31 J.-M. Li, H.-Y. Cheng, Y.-H. Chiu and Y.-J. Hsu, *Nanoscale*, 2016, **8**, 15720–15729.

32 Y.-C. Pu, H.-Y. Chou, W.-S. Kuo, K.-H. Wei and Y.-J. Hsu, *Appl. Catal., B*, 2017, **204**, 21–32.

33 Y.-H. Chiu and Y.-J. Hsu, *Nano Energy*, 2017, **31**, 286–295.

34 Y.-S. Chang, M. Choi, M. Baek, P.-Y. Hsieh, K. Yong and Y.-J. Hsu, *Appl. Catal., B*, 2018, **225**, 379–385.

35 J.-M. Li, C.-W. Tsao, M.-J. Fang, C.-C. Chen, C.-W. Liu and Y.-J. Hsu, *ACS Appl. Nano Mater.*, 2018, **1**, 6843–6853.

36 J.-M. Li, Y.-T. Wang and Y.-J. Hsu, *Electrochim. Acta*, 2018, **267**, 141–149.

37 Y.-H. Chiu, K.-D. Chang and Y.-J. Hsu, *J. Mater. Chem. A*, 2018, **6**, 4286–4296.

38 P.-Y. Hsieh, Y.-H. Chiu, T.-H. Lai, M.-J. Fang, Y.-T. Wang and Y.-J. Hsu, *ACS Appl. Mater. Interfaces*, 2019, **11**, 3006–3015.

39 Y.-S. Chang, P.-Y. Hsieh, T.-F. M. Chang, C.-Y. Chen, M. Sone and Y.-J. Hsu, *J. Mater. Chem. A*, 2020, **8**, 13971–13979.

40 W.-C. Hu, Y.-A. Chen, P.-Y. Hsieh, C.-W. Tsao, Y.-H. Chiu, T.-F. M. Chang, C.-Y. Chen, M. Sone and Y.-J. Hsu, *J. Taiwan Inst. Chem. Eng.*, 2020, **112**, 337–344.

41 A. Chauhan, M. Rastogi, P. Scheier, C. Bowen, R. Vasant Kumar and R. Vaish, *Appl. Phys. Rev.*, 2018, **5**, 041111.

42 W.-T. Chen, T.-T. Yang and Y.-J. Hsu, *Chem. Mater.*, 2008, **20**, 7204–7206.

43 T.-T. Yang, W.-T. Chen, Y.-J. Hsu, K.-H. Wei, T.-Y. Lin and T.-W. Lin, *J. Phys. Chem. C*, 2010, **114**, 11414–11420.

44 W.-T. Chen, Y.-K. Lin, T.-T. Yang, Y.-C. Pu and Y.-J. Hsu, *Chem. Commun.*, 2013, **49**, 8486–8488.

45 Y.-C. Pu, W.-T. Chen, M.-J. Fang, Y.-L. Chen, K.-A. Tsai, W.-H. Lin and Y.-J. Hsu, *J. Mater. Chem. A*, 2018, **6**, 17503–17513.

46 M.-Y. Kuo, C.-F. Hsiao, Y.-H. Chiu, T.-H. Lai, M.-J. Fang, J.-Y. Wu, J.-W. Chen, C.-L. Wu, K.-H. Wei, H.-C. Lin and Y.-J. Hsu, *Appl. Catal., B*, 2019, **242**, 499–506.

47 Y.-H. Chiu, S. A. Lindley, C.-W. Tsao, M.-Y. Kuo, J. K. Cooper, Y.-J. Hsu and J. Z. Zhang, *J. Phys. Chem. C*, 2020, **124**, 11333–11339.

48 A. Li, W. Zhu, C. Li, T. Wang and J. Gong, *Chem. Soc. Rev.*, 2019, **48**, 1874–1907.

49 R. Purbia and S. Paria, *Nanoscale*, 2015, **7**, 19789–19873.

50 H. Wang, Q. Tang, Z. Chen, T. Li and J. Wang, *Sci. China Mater.*, 2020, **63**, 2189–2205.

51 C. Xia, H. Wang, J.-K. Kim and J. Wang, *Adv. Funct. Mater.*, 2020, 2008247.

52 Q. Tang, Y. Ma and J. Wang, *Sol. RRL*, 2021, **5**, 2000443.

53 Y.-H. Chiu, T.-F. M. Chang, C.-Y. Chen, M. Sone and Y.-J. Hsu, *Catalysts*, 2019, **9**, 430.

54 Y.-H. Chiu, T.-H. Lai, M.-Y. Kuo, P.-Y. Hsieh and Y.-J. Hsu, *APL Mater.*, 2019, **7**, 080901.

55 P.-Y. Hsieh, J.-Y. Wu, T.-F. M. Chang, C.-Y. Chen, M. Sone and Y.-J. Hsu, *Arabian J. Chem.*, 2020, **13**, 8372–8387.

56 M.-J. Fang, C.-W. Tsao and Y.-J. Hsu, *J. Phys. D: Appl. Phys.*, 2020, **53**, 143001.

57 T.-H. Lai, K.-I. Katsumata and Y.-J. Hsu, *Nanophotonics*, 2020, **10**(2), 777–795.

58 C.-W. Tsao, M.-J. Fang and Y.-J. Hsu, *Coord. Chem. Rev.*, 2021, **438**, 213876.

59 G. D. Park, J.-K. Lee and Y. C. Kang, *Adv. Funct. Mater.*, 2017, **27**, 1603399.

60 G. D. Park and Y. C. Kang, *Small*, 2018, **14**, 1703957.

61 Y. Yin, R. M. Rioux, C. K. Erdonmez, S. Hughes, G. A. Somorjai and A. P. Alivisatos, *Science*, 2004, **304**, 711–714.

62 E. V. Shevchenko, M. I. Bondnarchuk, M. V. Kovalenko, D. V. Talapin, R. K. Smith, S. Aloni, W. Heiss and A. P. Alivisato, *Adv. Mater.*, 2008, **20**, 4323–4329.

63 Y.-H. Chiu, S. B. Naghadeh, S. A. Lindley, T.-H. Lai, M.-Y. Kao, K.-D. Chang, J. Z. Zhang and Y.-J. Hsu, *Nano Energy*, 2019, **62**, 289–298.

64 B. Zhao, X. Guo, W. Zhao, J. Deng, B. Fan, G. Shao, Z. Bai and R. Zhang, *Nano Res.*, 2017, **10**, 331–343.

65 Y. Lu, Y. Zhao, L. Yu, L. Dong, C. Shi, M.-J. Hu, Y.-J. Xu, L.-P. Wen and S.-H. Yu, *Adv. Mater.*, 2010, **22**, 1407–1411.

66 Q. Shi, P. Zhang, Y. Li, H. Xia, D. Wang and X. Tao, *Chem. Sci.*, 2015, **6**, 4350–4357.

67 J. Liu, L. Yu, C. Wu, Y. Wen, K. Yin, F.-K. Chiang, R. Hu, J. Liu, L. Sun, L. Gu, J. Maier, Y. Yu and M. Zhu, *Nano Lett.*, 2017, **17**, 2034–2042.

68 S. Xie, M. Jin, J. Tao, Y. Wang, Z. Xie, Y. Zhu and Y. Xia, *Chem.–Eur. J.*, 2012, **18**, 14974–14980.

69 Q. Xie, X. Zhang, H. Wu, X. Liu, G. Yue, Y. Yang and D.-L. Peng, *Electrochim. Acta*, 2014, **125**, 659–665.

70 H. Sun, Q. He, S. Zeng, P. She, X. Zhang, J. Li and Z. Liu, *New J. Chem.*, 2017, **41**, 7244–7252.

71 Y. Ye, L. Kuai and B. Geng, *J. Mater. Chem.*, 2012, **22**, 19132–19138.

72 Y. Zhang, C. Wang, H. Hou, G. Zou and X. Ji, *Adv. Energy Mater.*, 2016, **7**, 1600173.

73 M. Wang, J. Han, H. Xiong and R. Guo, *Langmuir*, 2015, **31**, 6220–6228.

74 J. Zhao, W. Li, L. Fan, Q. Quan, J. Wang and C. Xiao, *J. Colloid Interface Sci.*, 2019, **534**, 480–489.

75 G. Wan, X. Peng, M. Zeng, L. Yu, K. Wang, X. Li and G. Wang, *Nanoscale Res. Lett.*, 2017, **12**, 535.

76 X.-F. Wu, Y.-J. Wang, L.-J. Song, J.-Z. Su, J.-R. Zhang, Y.-N. Jia, J.-L. Shang, X.-W. Nian, C.-Y. Zhang and X.-G. Sun, *J. Mater. Sci.: Mater. Electron.*, 2019, **30**, 14987–14994.

77 S. H. Hwang, J. Yun and J. Jang, *Adv. Funct. Mater.*, 2014, **24**, 7619–7626.

78 Y. Li, L. Li, J. Hu and L. Yan, *Mater. Lett.*, 2017, **199**, 135–138.

79 J. Li, X. Li, X. Chen, Z. Yin, Y. Li and X. Jiang, *J. Colloid Interface Sci.*, 2019, **554**, 91–102.

80 Y. Chen, Z. Shi, Z. Wang, C. Wang, J. Feng, B. Pang, Q. Sun, L. Yu and L. Dong, *J. Alloys Compd.*, 2020, **829**, 154558.

81 Y. Li, Q. Shen, R. Guan, J. Xue, X. Liu, H. Jia, B. Xu and Y. Wu, *J. Mater. Chem. C*, 2020, **8**, 1025–1040.

82 M. Y. Son, Y. J. Hong, J.-K. Lee and Y. C. Kang, *Nanoscale*, 2013, **5**, 11592–11597.

83 J. Zhao, W. J. Li, L. P. Fan, Q. Quan, J. F. Wang and C. F. Xiao, *J. Colloid Interface Sci.*, 2019, **534**, 480–489.

84 M.-P. Liu, T. T. Su, L. Sun and H.-B. Du, *RSC Adv.*, 2015, **6**, 4063.

85 J. Zhou, L. Xu, J. L. Sun, D. P. He and H. Jiao, *Surf. Coat. Technol.*, 2015, **271**, 119126.

86 D. Wang, H. Zhang, J. Guo, H. Xu, X. Zhu and Z. Jiao, *RSC Adv.*, 2014, **4**, 37311–37319.

87 Z. F. Jiang, C. Z. Zhu, W. M. Wan, K. Qian and J. Xie, *J. Mater. Chem. A*, 2016, **4**, 1806.

88 K. J. Li, Y. Yang, A.-U.-R. Bacha, Y. Q. Feng, S. Ajmal, I. Nabi and L. W. Zhang, *Chem. Eng. J.*, 2019, **378**, 122191.

89 W. Wang, M. O. Tadéa and Z. P. Shao, *Chem. Soc. Rev.*, 2015, **44**, 5371–5408.

90 N. Wang, L. Ma, J. Wang, Y. Zhang and R. Jiang, *ChemPlusChem*, 2019, **84**, 1164–1168.

91 I. Khan, N. Sun, Y. Wang, Z. J. Li, Y. Qu and L. Q. Jing, *Mater. Res. Bull.*, 2020, **127**, 110857.

92 A. Khan, S. H. Zou, T. Wang, J. Ifthikar, A. Jawad, Z. W. Liao, A. Shahzad, A. Ngambiaa and Z. Q. Chen, *Phys. Chem. Chem. Phys.*, 2018, **20**, 13909.

93 Z. Chen, Y. T. Gao, D. Z. Mu, H. F. Shi, D. W. Lou and S. Y. Liu, *Dalton Trans.*, 2019, **48**, 3038.

94 W. Tu, Y. Zhou, H. Li, P. Li and Z. Zou, *Nanoscale*, 2015, **7**, 14232–14236.

95 M. Liang, T. Borjigin, Y. Zhang, H. Liu, B. Liu and H. Guo, *ACS Appl. Mater. Interfaces*, 2018, **10**, 34123–34131.

96 H. Liu, X. Meng, T. D. Dao, L. Liu, P. Li, G. Zhao, T. Nagao, L. Yanga and J. Ye, *J. Mater. Chem. A*, 2017, **5**, 10567–10573.

97 H. Wang, D. Wu, W. Wu, D. Wang, Z. Gao, F. Xu, K. Cao and K. Jiang, *J. Colloid Interface Sci.*, 2018, **539**, 194–202.

98 A. Ziarati, A. Badiei, R. Grillo and T. Burgi, *ACS Appl. Mater. Interfaces*, 2019, **11**, 5903–5910.

99 A. Fujishima and K. Honda, Electrochemical Photolysis of Water at a Semiconductor Electrode, *Nature*, 1972, **238**, 37–38.

100 X. W. Shi, Z. Z. Lou, P. Zhang, M. Fujitsuka and T. Majima, *ACS Appl. Mater. Interfaces*, 2016, **46**, 31738–31745.

101 R. J. Dillon, J.-B. Joo, F. Zaera, Y. Yin and C. J. Bardeen, *Phys. Chem. Chem. Phys.*, 2013, **15**, 1488–1496.

102 S. U. Lee, H. Y. Jung, D. H. Wi, J. W. Hong, J. H. Sung, S.-Il. Choi and S. W. Han, *J. Mater. Chem. A*, 2018, **6**, 4068.

103 X. Ma, K. Zhao, H. J. Tang, Y. Chen, C. G. Lu, W. Liu, Y. Gao, H. J. Zhao and Z. Y. Tang, *Small*, 2014, **10**, 4664–4670.

104 M. Waqas, S. Iqbal, A. Bahadur, A. Saeed, M. Raheel and M. Javed, *Appl. Catal., B*, 2017, **219**, 30–35.

105 P. S. Bassi, S. Y. Chiam, J. Barber and L. H. Wong, *ACS Appl. Mater. Interfaces*, 2014, **6**, 22490–22495.

106 Q. H. Liu, J. F. He, T. Yao, Z. H. Sun, W. R. Cheng, S. He, Y. Xie, Y. H. Peng, H. Cheng, Y. F. Sun, Y. Jiang, F. C. Hu, Z. Xie, W. S. Yan, Z. Y. Pan, Z. Y. Wu and S. Q. Wei, *Nat. Commun.*, 2014, **5**, 5122.

107 F. Su, S. C. Mathew, G. Lipner, X. Fu, M. Antonietti, S. Blechert and X. Wang, *J. Am. Chem. Soc.*, 2010, **132**, 16299–16301.

108 A. Tanaka, K. Hashimoto and H. Kominami, *J. Am. Chem. Soc.*, 2012, **134**, 14526–14533.

109 S. Yurdakal, G. Palmisano, V. Loddo, V. Augugliaro and L. Palmisano, *J. Am. Chem. Soc.*, 2008, **130**, 1568–1569.

110 N. Zhang, Y. H. Zhang, X. Y. Pan, X. Z. Fu, S. Q. Liu and Y. J. Xu, *J. Phys. Chem. C*, 2011, **115**, 23501–23511.

111 W. C. Peng, Y. Chen and X. Y. Li, *J. Hazard. Mater.*, 2016, **309**, 173–179.

112 H. Q. Wang, J. P. Yan, W. F. Chang and Z. M. Zhang, *Catal. Commun.*, 2009, **10**, 989–994.

113 K. Singha, A. Mondal, S. C. Ghosh and A. B. Panda, *Chem.–Asian J.*, 2017, **13**, 255–260.

114 M. Warrier, K. F. M. Lo, H. Monbouquette and M. A. Garcia-Garibay, *Photochem. Photobiol. Sci.*, 2004, **3**, 859–863.

115 J. Lee, J. C. Park and H. Song, *Adv. Mater.*, 2008, **20**, 1523–1528.

116 C. M. Fan, L. F. Zhang, S. S. Wang, D. H. Wang, L. Q. Lu and A. W. Xu, *Nanoscale*, 2012, **4**, 6835–6840.

117 M. Kim, J. C. Park, A. Kim, K. H. Park and H. Song, *Langmuir*, 2012, **28**, 6441–6447.

118 A. Ziarati, A. Badiei and R. Luque, *Appl. Catal., B*, 2018, **240**, 72–78.

119 S. Rohani, A. Ziarati, G. Mohammadi Ziarani, A. Badiei and T. Burgi, *Catal. Sci. Technol.*, 2019, **9**, 3820–3827.

120 A. Li, T. Wang, X. Chang, W. Cai, P. Zhang, J. Zhang and J. Gong, *Chem. Sci.*, 2016, **7**, 890–895.

121 Y. Liu, D. Zhang, Y. Shang, W. Zang and M. Li, *RSC Adv.*, 2015, **5**, 104785–104791.

122 A. Miyaura, K. Yamada and A. Suzuki, *Tetrahedron Lett.*, 1979, **20**, 3437–3440.

123 S. Gao, N. Shang, C. Feng, C. Wang and Z. Wang, *RSC Adv.*, 2014, **4**, 39242–39247.

124 M. Hosseini-Sarvari and Z. Bazyar, *ChemistrySelect*, 2018, **3**, 1898–1907.

125 N. Wang, L. Ma, J. Wang, Y. Zhang and R. Jiang, *ChemPlusChem*, 2019, **84**, 1164–1168.

126 V. Farina and B. Krishnan, *J. Am. Chem. Soc.*, 1991, **113**, 9585–9595.

127 C.-M. Huang, S.-H. Cheng, U.-S. Jeng, C.-S. Yang and L.-W. Lo, *Nano Res.*, 2012, **5**, 654–666.

128 W. Wang, S. Zhu, Y. Cao, Y. Tao, X. Li, D. Pan, D. L. Phillips, D. Zhang, M. Chen, G. Li and H. Li, *Adv. Funct. Mater.*, 2019, **29**, 1901958.

129 F. Zuo, K. Bozhilov, R. J. Dillon, L. Wang, P. Smith, X. Zhao, C. Bardeen and P. Feng, *Angew. Chem.*, 2012, **124**, 6327–6330.

130 M. Ohishi, M. Shiraishi, R. Nouchi, T. Nozaki, T. Shinjo and Y. Suzuki, *Jpn. J. Appl. Phys.*, 2007, **46**, 4170–4171.

131 W.-H. Lin, T.-F. M. Chang, Y.-H. Lu, T. Sato, M. Sone, K.-H. Wei and Y.-J. Hsu, *J. Phys. Chem. C*, 2013, **117**, 25596–25603.

132 H. S. Moon and K. Yong, *Appl. Surf. Sci.*, 2020, **530**, 147215.

133 R. Li, F. Zhang, D. Wang, J. Yang, M. Li, J. Zhu, X. Zhou, H. Han and C. Li, *Nat. Commun.*, 2013, **4**, 1432.

134 D. Wang, T. Hisatomi, T. Takata, C. Pan, M. Katayama, J. Kubota and K. Domen, *Angew. Chem., Int. Ed. Engl.*, 2013, **52**, 11252–11256.

135 J. Zhang, Z. Yu, Z. Gao, H. Ge, S. Zhao, C. Chen, S. Chen, X. Tong, M. Wang, Z. Zheng and Y. Qin, *Angew. Chem., Int. Ed. Engl.*, 2017, **56**, 816–820.

136 Z. Wang, W. Wu, Q. Xu, G. Li, S. Liu, X. Jia, Y. Qin and Z. L. Wang, *Nano Energy*, 2017, **38**, 518–525.

137 P. She, H. Rao, B. Guan, J. S. Qin and J. Yu, *ACS Appl. Mater. Interfaces*, 2020, **12**, 23356–23362.

138 D. Zheng, X.-N. Cao and X. Wang, *Angew. Chem.*, 2016, **128**, 11684–11688.

139 Q. M. Sun, N. Wang, J. H. Yu and J. C. Yu, *Adv. Mater.*, 2018, **30**, 1804368.

140 A. Li, X. Chang, Z. Huang, C. Li, Y. Wei, L. Zhang, T. Wang and J. Gong, *Angew. Chem., Int. Ed. Engl.*, 2016, **55**, 13734–13738.